MIT Open Access Articles

Two-phase modeling of sediment clouds

The MIT Faculty has made this article openly available. *Please share* how this access benefits you. Your story matters.

Citation	Lai, Adrian C. H., Bing Zhao, Adrian Wing-Keung Law, and E. Eric Adams. "Two-Phase Modeling of Sediment Clouds." Environ Fluid Mech 13, no. 5 (February 12, 2013): 435–463.
As Published	http://dx.doi.org/10.1007/s10652-013-9271-x
Publisher	Springer Netherlands
Version	Author's final manuscript
Citable link	http://hdl.handle.net/1721.1/104082
Terms of Use	Article is made available in accordance with the publisher's policy and may be subject to US copyright law. Please refer to the publisher's site for terms of use.

Massachusetts Institute of Technology

DSpace@MIT

Two-phase modeling of sediment clouds

Adrian C.H. Lai[1], Bing Zhao[2], Adrian Wing-Keung Law[3], and E. Eric Adams[4]

Abstract: A sediment cloud release in stagnant ambient fluid occurs in many engineering applications. Examples include land reclamation and disposal of dredged materials. The detailed modeling of the distinct characteristics of both the solid and fluid phases of the sediment cloud is hitherto unavailable in the literature despite their importance in practice. In this paper, the two-phase mixing characteristics of the sediment cloud are investigated both experimentally and theoretically. Experiments were carried out to measure the transient depth penetration, and the lateral spread of the sediment cloud and its entrained fluid using the laser induced fluorescence technique, with a range of particle sizes frequently encountered in the field (modeled at laboratory scale). A two-phase model of the sediment cloud that provides detailed predictions of the mixing characteristics of the individual phases is also proposed. The entrained fluid characteristics are solved by an integral model accounting for the buoyancy loss (due to particle separation) in each time step. The flow field induced by the sediment cloud is approximated by a Hill's spherical vortex centered at the centroid and with the size of the entrained fluid. The particle equation of motion under the effect of the induced flow governs each computational particle. A random walk model using the hydrodynamic diffusion coefficient is used to account for the random fluctuation of particles in the dispersive regime. Overall, the model predictions of the two-phase mixing characteristics are in good agreement with the experimental data for a wide range of release conditions.

Keywords: two-phase flows; particle clouds; thermals; sediment disposal; land reclamation; dredging

1Center for Environmental Sensing and Modeling, Singapore-MIT Alliance for Research and Technology Centre, 1 CREATE Way, Singapore 138602. Email: adrian.lai@smart.mit.edu

2 School of Civil and Environmental Engineering, Nanyang Technological University, 50 Nanyang Avenue, 639798 Singapore. Email: zhao0129@e.ntu.edu.sg

3 School of Civil and Environmental Engineering, Nanyang Technological University, 50 Nanyang Avenue, 639798 Singapore. Email: cwklaw@ntu.edu.sg

4 Department of Civil and Environmental Engineering, Massachusetts Institute of Technology, Cambridge, MA 02139, USA. Email: eeadams@mit.edu

1 Introduction

An instantaneous release of sediment into a fluid occurs in many engineering applications. During land reclamation, sand is commonly dumped into coastal waters to create land mass (Zhao et al. 2012). Coarser dredged materials such as rubble are also disposed in designated areas of lakes and coastal waters (Buhler and Papantoniou 1999); and fine sediment is used to cap confined aquatic disposal cells containing contaminated materials (Ruggaber 2000). For environmental impact assessment, as well as to plan for the disposal operations, it is necessary to predict the fate and transport of the sediment cloud. An issue which is related to the analysis of sediment clouds, but that receives little attention, is the fate and transport of the interstitial fluid. It can be of significant environmental importance - for example the transport of dissolved pollutants in the interstitial fluid is driven by the motion of the sediment cloud.

Released sediment clouds typically set the surrounding ambient fluid into motion. Ambient fluid is drawn into the sediment cloud through turbulent entrainment, and the mixing characteristics such as the radius, and descent velocity of the cloud change as a result. The volume of entrained fluid grows and descends along with the sediment cloud forming a solid-fluid two-phase flow, the carrier and dispersed phase being the entrained fluid and the sediment particle respectively. The two-phases separate when the fluid velocity decreases to the order of the settling velocity of particles comprising the cloud (Rahimipour and Wilkinson 1992). After the phase separation, the sediment cloud continues to descend at approximately the settling velocity of the individual particles, while the entrained fluid descends as a puff (Bush et al. 2003).

There have been many studies concerning the instantaneous release of sediment clouds. Rahimipour and Wilkinson (1992) suggested that the behavior of sediment clouds during their descent can be separated into three phases: (i) the initial acceleration phase - when the sediment cloud accelerates from rest to its maximum velocity; (ii) the self-preserving phase - when the cloud can be approximated as a spherical miscible thermal (Scorer 1957, Turner 1973) with buoyancy given by the particles; and finally (iii) the dispersive regime - when the cloud settles as a bowl shaped swarm with all particles moving almost vertically downwards. A cloud number was defined as the ratio of the particle settling velocity and the cloud characteristic velocity to study the behavior of the sediment cloud:

$$N_c = w_s r_s (\frac{\rho_a}{B_o})^{1/2}$$

Where w_s is the particle settling velocity, r_s is the half-width of the sediment cloud, ρ_a the ambient density, and B_o the sediment cloud initial buoyancy. When N_c<1 the sediment cloud is in the thermal regime, it then enters the dispersive regime when N_c>1. The delineation of the phases can alternatively be determined using a length scale analysis (Luketina and Wilkinson 1998). A similar length scale analysis for line sediment clouds was done by Noh and Fernando (1993).

At present, most mathematical models for sediment clouds use the integral model approach, in which the sediment cloud is treated as an equivalent miscible thermal for analysis. Solving the conservation of mass, momentum, and buoyancy equations, together with the entrainment hypothesis (Morton et al. 1956) gives the essential bulk characteristics of the cloud. The flow pattern induced by a thermal was studied theoretically by Turner (1964) using an expanding Hill's spherical vortex. Buhler and Papantoniou (2001) developed separate integral equations for the self-preserving and dispersive regimes. The resulting growth and velocity relationships with the cloud penetration depth showed good agreement with their experimental data. Bush et al. (2003) developed an integral model to account for the effect of linear ambient stratification, and was able to predict the growth and velocity changes of a sediment cloud in the thermal regime. Recent studies focused on including the effects of initial release conditions to the sediment cloud development. Ruggaber (2000) considered the effect of moisture content, and found that the mixing characteristics of the cloud are insensitive to many conditions encountered in practice. Zhao et al. (2012) included the effect of initial release height on the cloud development in the thermal regime through virtual origin corrections. While traditional integral models are able to give accurate solutions to the bulk characteristics of the sediment cloud in the thermal regime, they are in general not applicable in the dispersive regime, where changes in the cloud characteristics appear to be due to the random motion of individual particles (e.g. Ruggaber 2000) rather than turbulent entrainment. The characteristics of the entrained fluid are also not predicted. It is also difficult with existing models to simulate sediment clouds with multiple particle sizes, as are frequently encountered in practice.

A number of computational fluid dynamics (CFD) studies revealed further details of sediment clouds. Li (1997) developed a CFD model that treated the discrete particles as a continuous density field, and used a mixing length model for turbulence closure. The turbulence coefficients were approximated by calibration with the previous experimental data of Scorer (1957). Li's results revealed the vortex motion (as in a vortex ring) for fine particles with small settling velocity.

Gu and Li (2004) developed an Eulerian-Lagrangian CFD model to study sediment clouds with multiple particle sizes. The motion of the fluid phase was computed by a two-equation turbulence model, while the motion of solid phase (particles) was computed by assuming the particle velocity to be the sum of a fluid random velocity and the particle settling velocity. The two-phases were coupled using the multiphase particle-in-cell method. The resulting cloud velocity and growth were in agreement with their experiments of multiple sizes sediment cloud releases. Multiphase CFD models are considered to be currently still in development stage.

Previous theoretical and experimental investigations had focused primarily on the sediment cloud thermal regime, while the fluid motion induced by the sediment cloud was rarely studied. In this paper, we first introduce Turner (1964)'s expanding Hill's spherical vortex model for studying the flow structure of a single phase thermal. Then we extend Turner's model and propose a two-phase model of the solid-fluid flow to solve for the transport of both particles and entrained fluid in the thermal and dispersive regimes. Experiments measuring both the solid and fluid phase characteristics were conducted to validate the model. Comparisons of model predictions with observations from previous studies also demonstrate the generality of the model.

2 Modeling of a single phase thermal

2.1 An expanding Hill's vortex

For later model development, it is useful to first consider an expanding Hill's vortex model which Turner (1964) used to study the flow induced by a single-phase thermal.

Hill's vortex (1894) is an exact solution to Euler's equation, which describes the flow induced by a steady non-expanding vortex ring with vorticity distributed in a sphere (see Appendix A). While useful for studying the flow induced by a vortex ring, the Hill's vortex is not suitable for studying the thermal flow since entrainment is not modeled.

Turner (1964) then proposed an extension to the Hill's vortex solution such that the flow pattern of a thermal can be studied. With a priori specification of the Hill's vortex radius as a function of time ($r = \alpha\, t$, where α is the entrainment coefficient), Turner assumed the instantaneous flow induced by a thermal is the same as that of this expanding Hill's vortex. The entrainment pattern of a thermal can be studied by computing the trajectory of a layer of inertialess particles when an expanding Hill's spherical vortex passes through. Results of Turner showed that it had reasonable resemblance to the experimental observation of a thermal structure.

Figure 1 shows an example trajectory of a layer of 12 particles. Particles are located at $z = 2r_o$, with equal spacing spanning a width of $4r_o$, where r_o is the initial radius of the thermal with volume 8.42×10^{-5} m^3. An expanding spherical vortex with growth rate $r = \alpha\, t$ passes through from negative to positive z with unit velocity starting from $z_o =0$, $t_o = r_o/\alpha$. The dimensions have been scaled such that the sphere is fixed in size in the plot. Results using α=0.25 are shown. Solid lines represent results by solving Turner's derived equations, while circle symbols represent our computation by advecting particles numerically with the flow field induced by the same expanding spherical vortex. The two results are visually indistinguishable. The number of particles being entrained can be shown to increase with α.

2.2 Continuity of an expanding Hill's vortex

Two issues were not considered in Turner's model. Firstly, a thermal does not descend with a constant velocity, but decelerates during its descent. Secondly, the continuity issue of whether the modeled entrainment into a thermal equals the thermal growth was not addressed. This section serves to resolve these two issues.

The thermal motion and its velocity during its descent can be predicted by solving an integral model (e.g. Escudier and Maxworthy 1973) describing the conservation of volume, momentum, and buoyancy of a thermal (see section 3.1 for details). Equation (1) in particular describes the change of thermal volume over time being equal to the entrainment into the thermal.

The conservation of volume equation can also be considered in the expanding Hill's vortex model. Instead of assuming the thermal velocity to be a constant, in our model we have used the velocity that is predicted by the integral model; the integral model also predicts the radius r_i of the thermal. A numerical experiment is performed to determine whether the conservation of volume is satisfied. A numerical tank of volume V is considered to be filled with N 'water parcels', each with volume V/N. As an expanding spherical vortex passes through, some of the parcels will be entrained, and these will be 'relabelled' as 'thermal parcels'(Figure 2). (Scase et al. 2007 considered a similar example for pure plumes.) The number of parcels and the total volume contained within a thermal represented as an expanding spherical vortex of radius r_h are tracked in each time step, and compared with the thermal volume predicted by the integral model.

Results show that if $r_h = r_i$ is assumed, the volume of the expanding Hill's vortex model is about 4% less than that of the integral model, indicating that the characteristic width of an expanding Hill's vortex can be different between the two. This can be expected as the two models have markedly different assumptions regarding the velocity distributions within and outside the thermal. Because $r_h \neq r_i$, an adjustment factor η, such that $r_h = \eta\, r_i$, needs to be employed for the volume to be conserved.

We determined the optimum η to be 1.012, and with this adjustment, the volume difference for every time step was generally less than 0.5%, easily sufficient for practical purposes (the corresponding difference in radius being less than 0.2%). Figure 3 shows a comparison of the thermal volume predicted by an integral model, and by an expanding Hill's vortex with $\eta = 1.012$. There is practically no difference between them. For consistency purposes, in all following sections the modeled half-width of the thermal will be taken as that predicted by the integral model.

3 Two-phase modeling of sediment clouds

We now extend Turner (1964)'s model of a single-phase thermal to a two-phase sediment cloud. The problem under consideration is shown in Figure 4. Each of the N_p spherical particles with diameter d, mass m_p, and density ρ_p , are released instantaneously (in the $+z$ direction) into an otherwise stagnant ambient of density ρ_a. The total initial mass of the sediment cloud is m_o, and the total buoyancy of the cloud is $B_o = m_o(1- \rho_a /\rho_p)g$, where g is the acceleration due to gravity. Initially, it is assumed that the sediment cloud has a half-width r_s and front position z_s equal to the entrained fluid half-width r_f and front position z_f (approximated as a sphere with z_c denoting its centroid vertical coordinate). The entrained fluid is composed of the original tracer mixed with the sediment particles before release, and the ambient fluid entrained by turbulent entrainment. As the cloud descends, the mixing characteristics of the two phases are expected to differ increasingly. The objective is to predict the change in these characteristics of the two phases throughout the descent process.

3.1 Modeling of the fluid motion

Initially, when the particles are all within the entrained fluid, the motion of the entrained fluid can be described by an integral model tracking the changes in its volume V, momentum M, and buoyancy B. Over time, particles gradually settle out, and the buoyancy B of the entrained fluid is expected to decrease. By assuming a constant circulation (K) in the sediment cloud, Turner (1957) showed that $B = B_o = 2\pi c\alpha\rho_a K^2$ in the thermal regime, where c is a constant depending on the thermal shape, and α is the entrainment coefficient. In the dispersive regime, B is expected to be 0 as the sediment particles have completely separated from the entrained fluid. Further, Rahimipour and Wilkinson (1992) obtained experimentally the variation of α in the thermal regime in the form of $\alpha = \alpha_0 (1- c_1 N_c^{c2})$, where α_0 is the initial entrainment coefficient, c_1 and c_2 are experimental constants. This results in the following integral equations describing the bulk characteristics of the entrained fluid:

$$\frac{dV}{dt} = 4\pi\alpha r_f{}^2 w_f \qquad (1)$$

$$\frac{dM}{dt} = \frac{d}{dt}[w_f V(\rho_f + C_M\rho_a)] = B - \frac{1}{2}C_D\pi\rho_a r_f{}^2 w_f{}^2 \qquad (2)$$

$$\frac{dz_c}{dt} = w_f \qquad (3)$$

$$B = \begin{cases} B_o(1 - c_1 N_c{}^{c2}) & \text{when} \quad N_\mathrm{c} \le 1 \\ 0 & \text{when} \quad N_\mathrm{c} > 1 \end{cases} \qquad (4)$$

where w_f, ρ_f, and V are the characteristic velocity, `density', and volume of the entrained fluid respectively; $C_M \approx 0$ (Bush et al. 2003) is the added mass coefficient; $C_D \approx 0$ (Ruggaber 2000) is the drag coefficient. We have assumed in the model that the dispersive regime is reached when $N_c = 1$ (e.g. Bush et al. 2003).

The following two equations are used to relate the characteristic variables to the bulk characteristics of the entrained fluid (with the Boussinesq approximation):

$$r_f = (\frac{3V}{4\pi})^{1/3} \qquad (5)$$

$$w_f = \frac{M}{\rho_f V} \approx \frac{M}{\rho_a V} \qquad (6)$$

Equations (1) – (3) are solved using a fourth-order Runge-Kutta numerical integration scheme, and the algebraic expressions equations (4) – (6) with initial conditions ($V = 0$, $M = 0$, $z_f = z_{vo}$) at $t = t_{vo}$ which can be determined with a known virtual origin in space and time (z_{vo}, t_{vo}). An additional equation of tracer mass conservation

$$\frac{d(VC)}{dt} = 0$$

(where C is the volumetric mean concentration of the entrained fluid) can be used to compute the dilution of the tracer that descends along with the sediment cloud.

Turner (1964) suggested that the flow field of the thermal resembles that of an expanding Hill's spherical vortex (Hill 1894) with buoyancy conservation. We adopt a similar but new approach to the sediment cloud by assuming that the entrained fluid is a thermal with reducing buoyancy as shown in equation (4). Thus, the instantaneous flow field [u_z (z,r), u_r (z,r)] at a particular time t can be represented as a Hill's vortex centered at (z_c, 0) with constant velocity w_f and radius r_f. This yields the following analytical expressions for the complete fluid flow field at time t:

Inside the entrained fluid ($R<r_f$, where $R^2 = r^2 + (z - z_c)^2$)

$$u_z = -\frac{3w_f}{4}[4(\frac{r}{r_f})^2 + 2(\frac{z - z_c}{r_f})^2 - \frac{10}{3}] \qquad (7)$$

$$u_r = \frac{3w_f}{2r_f^{\ 2}} r(z - z_c) \qquad (8)$$

Outside the entrained fluid ($R> r_f$):

$$u_z = \frac{w_f r_f^{\ 3}}{2} \frac{2(z - z_c)^2 - r^2}{[(z - z_c)^2 + r^2]^{5/2}} \qquad (9)$$

$$u_r = \frac{3w_f r_f^{\ 3} r(z - z_c)}{2[(z - z_c)^2 + r^2]^{5/2}} \qquad (10)$$

3.2 Modeling of the particle motion

3.2.1 Particle equation of motion

A Lagrangian approach is used to model the sediment particle motion. With the computed fluid flow field, the particle equation of motion (e.g. Crowe et al. 1998, Lee 2010) can be used to compute the hydrodynamic forces acting on each particle:

$$m_p \frac{d\overrightarrow{u_p}}{dt} = \overrightarrow{F_D} + \overrightarrow{F_A} + \overrightarrow{F_{SG}} + \overrightarrow{F_g} \quad (11)$$

where

$\overrightarrow{F_D} = 3\pi\mu(\overrightarrow{u_f} - \overrightarrow{u_p})\frac{C_{Dp}\,\mathrm{Re}_p}{24}$ is the drag force; $\overrightarrow{F_A} = \rho_f V_p (\frac{D\overrightarrow{u_f}}{Dt} - \frac{d\overrightarrow{u_p}}{dt})$ is the added mass force; $\overrightarrow{F_{SG}} = \rho_f V_p (\frac{D\overrightarrow{u_f}}{Dt} + g)$ is the fluid stress gradient; $\overrightarrow{F_g} = -\rho_p V_p \vec{g}$ is the gravitational force; $\overrightarrow{u_f} = (u_z, u_r)$ is the fluid velocity; $\overrightarrow{u_p} = (u_{pz}, u_{pr})$ is the particle velocity; μ is the dynamic viscosity of the fluid; C_{Dp} is the drag coefficient of a particle; $\mathrm{Re}_{Dp} = \frac{|\overrightarrow{u_f} - \overrightarrow{u_p}|d}{\nu}$ is the particle Reynolds number ($\nu = \mu / \rho_f$); and V_p is the volume of a particle.

The drag coefficient can be evaluated by the formula from Swamee and Ojha (1991):

$$C_{Dp} = 0.5\{16[(\frac{24}{\mathrm{Re}_p})^{1.6} + (\frac{130}{\mathrm{Re}_p})^{0.72}]^{2.5} + [(\frac{40000}{\mathrm{Re}_p})^2 + 1]^{-0.25}\}^{0.25}$$

Simplifying and casting equation (11) into a component form:

$$(1+\frac{\rho_f}{2\rho_p})\frac{d^2 r_p}{dt^2} = 3\pi\mu d(u_r - u_{pr})\frac{C_{Dp}\,\mathrm{Re}_p}{24\rho_p V_p} + \frac{3\rho_f}{2\rho_p}\frac{Du_r}{Dt} \qquad (12)$$

$$(1+\frac{\rho_f}{2\rho_p})\frac{d^2 z_p}{dt^2} = 3\pi\mu d(u_z - u_{pz})\frac{C_{Dp}\,\mathrm{Re}_p}{24\rho_p V_p} + \frac{3\rho_f}{2\rho_p}\frac{Du_z}{Dt} - g(1-\frac{\rho_f}{\rho_p}) \quad (13)$$

The convective derivatives in equations (12) and (13) can be expressed as (e.g. Batchelor 1967):

$$\frac{Du_z}{Dt} = \frac{\partial u_z}{\partial t} + (\frac{\partial u_z}{\partial z} + \frac{\partial u_r}{\partial r} + \frac{u_r}{r})u_z$$

$$\frac{Du_r}{Dt} = \frac{\partial u_r}{\partial t} + (\frac{\partial u_z}{\partial z} + \frac{\partial u_r}{\partial r} + \frac{u_r}{r})u_r$$

The partial derivatives above can be evaluated analytically using the Hill's vortex velocity field (see Appendix A) as follow:

Inside the entrained fluid ($R<r_f$):

$$\frac{\partial u_z}{\partial z} = -\frac{3w_e(z-z_c)}{{r_f}^2}; \qquad \frac{\partial u_z}{\partial t} = \frac{3u_z}{{r_f}^2}(z-z_c) \; (14)$$

$$\frac{\partial u_r}{\partial r} = \frac{3w_f(z-z_c)}{2{r_f}^2}; \qquad \frac{\partial u_r}{\partial t} = -\frac{3{w_f}^2}{2{r_f}^2}r \qquad (15)$$

Outside the entrained fluid ($R>r_f$):

$$\frac{\partial u_z}{\partial z} = -\frac{3w_f{r_f}^3}{2}\frac{(z-z_c)[2(z-z_c)^2-3r^3]}{\left[(\mathrm{z}\text{-}\mathrm{z_c})^2+r^2\right]^{7/2}}; \qquad \frac{\partial u_z}{\partial t} = \frac{3{w_f}^2{r_f}^3}{2}\frac{(z-z_c)[2(z-z_c)^2-3r^3]}{\left[(\mathrm{z}\text{-}\mathrm{z_c})^2+r^2\right]^{7/2}}$$

(16)

$$\frac{\partial u_r}{\partial r} = \frac{3w_f{r_f}^3}{2}\frac{(z-z_c)[2(z-z_c)^2-4r^2]}{\left[(\mathrm{z}\text{-}\mathrm{z_c})^2+r^2\right]^{7/2}}; \qquad \frac{\partial u_r}{\partial t} = \frac{3{w_f}^2{r_f}^3}{2}\frac{r[4(z-z_c)^2-r^2]}{\left[(z-z_c)^2+r^2\right]^{7/2}}$$

(17)

Equations (14) – (17) are evaluated at the position of each particle $z=z_p$ and $r=r_p$. Equations (12) – (13) can be cast into a set of ordinary differential equations which is solved by a fourth order Runge-Kutta integration scheme:

$$\frac{du_{pr}}{dt}=\frac{A(u_r-u_{pr})+\dfrac{3}{2}\dfrac{\rho_f}{\rho_p}\dfrac{Du_r}{Dt}}{1+\dfrac{\rho_f}{2\rho_p}} \qquad (18)$$

$$\frac{du_{pz}}{dt}=\frac{A(u_z-u_{pz}-B)+\dfrac{3}{2}\dfrac{\rho_f}{\rho_p}\dfrac{Du_z}{Dt}}{1+\dfrac{\rho_f}{2\rho_p}} \qquad (19)$$

$$\frac{dr_p}{dt}=u_{rp} \qquad (20)$$

$$\frac{dz_p}{dt}=u_{zp} \qquad (21)$$

where $A=\dfrac{\pi\mu d C_{Dp}\operatorname{Re}_p}{8m_p}$, and $B=g(1-\dfrac{\rho_f}{\rho_p})/(\dfrac{\pi\mu C_{Dp}\operatorname{Re}_p}{8m_p})$.

These equations are subject to initial conditions $(z_{po},r_{po},u_{pzo},u_{pro})$ at $z_c=0$, $t=0$, where a uniform particle distribution (equidistance in z- and r- direction) in the spherical entrained fluid of half-width w_f (t=0) is assumed.

3.2.2 Hydrodynamic diffusion of particles in the dispersive regime

In the dispersive regime, the sediment cloud descends as a swarm with velocity being the same as the settling velocity of an individual particle. At the same time, the swarm continues to spread laterally, though at a smaller rate than in the thermal regime. Buhler and Papantoniou (1991) suggested $\alpha\approx0.1$, arguing that the spreading of the particles is caused by the lateral displacement flow resulting from the wake behind each particle. Rahimipour and Wilkinson (1992) suggested that the spread in the dispersive regime is due to the weak dispersive influences between adjacent particles. However, so far no study has confirmed the physical mechanism for the lateral spread of a sediment cloud in the dispersive regime. Here, it is suggested that the sediment cloud spread is due to `hydrodynamic diffusion' (Guazzelli and Hinch 2010) as seen in a group of settling particles. It has been observed that the random motion of each particle in a group causes the group to spread even when the particle volume fraction is small.

The normalized hydrodynamic diffusivity in the vertical direction $D_v/[(d/2)\ w_s]$ as a function of particle volume fraction was reported previously by Davis and Hassen (1988, 1989). In our model, the particle volume fraction in each time step is computed by assuming the sediment cloud volume as $(4/3)\eta\pi r^3$, where $\eta= 0.68$ is the shape factor (Zhao et al. 2012). $D_v/[(d/2)\ w_s]$ can hence be determined by implementing Davis and Hassen’s plots in our model (for our experiments the typical value of the normalized hydrodynamic diffusivity is in the order of 0.7). The normalized hydrodynamic diffusivity in the horizontal direction $D_h/[(d/2)\ w_s]$ was found to be a few times smaller than than the normalized vertical diffusivity, and by using data of Nicolai et al. (1995) for particle volume fraction <0.2, the ratio is computed to be $D_v / D_h = 3.7$. In the above expressions, w_s is the settling velocity of the particle which can be estimated experimentally, or by Dietrich (1982)'s formula for spherical spheres (Appendix B). The settling velocity is that for an isolated particle, as a dilute suspension is considered (volume fraction in the order of 0.001); hindered settling is not considered but its affect is expected to be small for a dilute suspension. The hydrodynamic diffusion effect can be incorporated into the model by a random walk model (Kitanidis 1994):

$$r_p(t+\Delta t) = r_p(t) + u_{pr}\Delta t + \xi\sqrt{2D_h\Delta t} \quad (22)$$

$$z_p(t+\Delta t) = z_p(t) + u_{pz}\Delta t + \xi\sqrt{2D_v\Delta t} \qquad (23)$$

where ξ is a normally distributed random number with mean 0 and variance 1. Note that in the dispersive regime, it is assumed that the vorticity generated is only in the fluid phase (or the entrained fluid) represented by the expanding Hill's vortex. From the simulation of Pignatel et al. (2011) using Oseenlets with the particle Reynolds number in the order of $\mathrm{Re_p} \sim O(0.1)$, it can be seen that weak vorticity can also be present within the particle cloud, even in the dispersive regime. Such vorticity is due to the macroscopic effect induced by each particle, which can affect their settling. We do not preclude the possibility of similar macroscopic effects from particles which generate vorticity in our study of high particle Reynolds number flows [$\mathrm{Re_p} \sim O(100)$], but experimental observations show that this effect is relatively weak, as all particles fall almost vertically. Also, note that our primary objective is not to model the sediment cloud motion in such details, but to provide an efficient tool for predicting its bulk characteristics. The effectiveness of the present modeling approach can ultimately be determined by comparison with experiments.

3.3 Model implementation details

Given the total mass of a sediment cloud and the particle diameter, the motion of both the fluid and solid particles can be predicted by the model in the following manner. First, the time step used in the model is $\Delta t = 0.05 r_o / w_{\max}$, where $r_o = [3V_p/(4\pi)]^{1/3}$ is the equivalent radius of the initial sediment cloud volume, and w_{max} is approximately the maximum velocity that a thermal can attain in the initial acceleration regime, which can be estimated to be (Escudier and Maxworthy 1973, see Appendix C):

$$w_{\max} = \sqrt{\frac{g r_o (\rho_p - \rho_a)/\rho_a}{2\alpha}} \frac{1}{(1-(\rho_p - \rho_a)/\rho_a)^{1/3}} \tag{24}$$

Physically, the chosen Δt roughly assumes that the movement of particles at any time is less than 0.05 r_o. Further reducing the time step does not yield noticeable changes in the predicted results for the cases considered in this study.

The solution scheme for the model can be expressed as a simple algorithm:

1. Determine the initial conditions of entrained fluid at $z = 0$, $t = 0$ from virtual origin;
2. Distribute the particles with the determined initial conditions at $z = 0$, $t = 0$;
3. Use the integral model to solve for the entrained fluid characteristics;
4. Compute the velocity field induced by an expanding Hill's vortex;
5. Compute the total acceleration and forces acting on the particles;
6. Account for the hydrodynamic diffusion of the particles in the dispersive regime;
7. Solve the particle tracking equation;
8. Advance to next time step and repeat from step 3 until the desired time duration is reached.

With a known virtual origin length above the water surface z_{vo}, the integral model (Equations (1) – (3)) can be used to determine the virtual time origin t_{vo} assuming a constant buoyancy. The initial conditions of the entrained fluid at the real origin z=0 and t=0 are then known (Zhao et al. 2012). Particles ($N_p \approx 500$ in this study) are uniformly distributed inside the entrained fluid at t=0 (particle spacing is equal in r- and z- directions within the sphere of radius r_o).

Here we have used the concept of "computational particles" (Crowe et al. 1998), whereby the model identifies a packet of particles as a single computational particle with the same properties as the physical particles. The actual number of particles is in the order of 10000 – 20000. Using the actual number of particles only increases computational time and our results show that increasing N_p beyond about 500 produced no noticeable change in the prediction results.

4 Experiments

4.1 Experimental setup

Because experiments on the two-phase characteristics of a sediment cloud were limited in the literature, a comprehensive experimental programme was carried out in the present study for this purpose.

Experiments were carried out in a 0.85 m (width) × 2.85 m (length) × 1.0 m (depth) glass tank. The schematic diagram of the experimental setup is shown in Figure 5. A constant mass of 3.0 g particles (Ballotini Impact beads, Potters Industries, Inc.) was filled in a cylinder with 0.9 cm inner radius (r_c) in all experiments. Three sizes of particle were considered: size A with a median diameter d= 0.725 mm; B: 0.513 mm; and D: 0.256 mm. All particles had a density of 2.5 g/cm^3 (Table 1). The range of particle size can be scaled up to that typically encountered in the field by using Froude scaling (Ruggaber 2000). The cylinder was placed at the mid-width of the tank. Rhodamine-B (Rho-B) dye solution was added to visualize the entrained fluid. The level of the dye solution coincided with the water level external to the cylinder so there was no extra pressure acting on the particle-dye mixture. The cylinder bottom was covered with a taut latex sheet, which could be ruptured quickly for an instantaneous release. A needle, placed at the center of the cylinder was used to rupture the latex sheet. It was controlled by an electrically triggered motor to eliminate human factors affecting the release conditions. The minimum distance from the cylinder center to the tank wall was 0.425 m, which was sufficient for the experiments in this study to be free from boundary effects.

Laser induced fluorescence (LIF) was used to visualize both the sediment cloud and the entrained fluid. A laser sheet, with approximately 3 mm thickness, was generated using a 532 nm solid state diode pump laser and a diverging lens located at the bottom of the tank with its convex side facing upwards. It cut through the plane of symmetry of the cylinder and was wide enough to cover the area of interest. With the illumination, Rho-B dye fluoresced to give out yellow light and the particle diffracted the green laser light towards the camera.

Two 8-bit monochrome CCD cameras (Dantec FlowSense 2M, 1186×1600 pixels) and a color video camera (Sony HDR-XR550E, 1080×1440 pixels) were used in all experiments. One CCD camera was used to capture the LIF images at 15 Hz of the dyed entrained fluid by fitting a 570 nm lowpass filter. Another CCD camera was used to capture the sediment particle images by fitting a 532 nm bandpass filter. Both cameras were aligned perpendicular to the laser sheet. The sediment cloud motion in the upper region (close to the release point) and the lower region close to the bottom were captured in separate experiments due to the limited field of view of the CCD camera. The video camera perpendicular to the laser sheet was also used to capture the motion and provide extra information of the sediment cloud release outside the field of view. Recording began just before the rupture of the latex sheet, and stopped when the entrained fluid reached the tank bottom. Experiments were repeated 10 times [5 for upper region (z ~ 0 -30 cm) and 5 for lower region (z ~ 30 - 60 cm)] for all sizes of particle. The captured LIF images were background subtracted for analysis. The captured videos were also converted to a series of 30 Hz 24-bit images (8 bits for each red, green and blue) for analysis.

4.2 Observations

It is useful to define two length scales for describing the behavior of a sediment cloud (Luketina and Wilkinson 1998): $l_{at} = (m_o/\rho_f)^{1/3}$ is the acceleration-to-thermal regime length scale, and is approximately the distance for the cloud to enter the thermal regime; $l_{td} = [(m_o/\rho_f)g']^{1/2}/w_s$ is the thermal-to-dispersive regime length scale, and is the approximate distance required for the cloud to reach the dispersive regime. These two length scales are computed and listed in Table 1.

Two-phase sediment clouds were observed in all experiments. The typical observation in an experimental run can be seen in Figure 6. In the current experiments, l_{at} was relatively short such that the sediment clouds entered the thermal regime almost immediately after being released. Figure 6(*a*) shows that in the beginning, the particles stayed with the entrained fluid and descended as a coherent mass resembling a thermal. A buoyant vortex ring structure was evident in many cases. A trailing stem of the fluid phase was generally formed, but the mass of particles in the stem appeared significant only for smaller sizes of particle considered (see Ruggaber (2000) for a detailed account of the particle trailing stem formation). Figure 6(*b*) shows that the particles began to settle out from the entrained fluid, with the particles concentrated at the bottom of the thermal. This occurred approximately at $z \approx l_{td}$ to 2 l_{td}. After separation, the particles continued to descend at approximately their own settling velocity. Meanwhile the entrained fluid descended with its remaining momentum imparted by the particles; a vortex ring structure was sometimes observed (like a puff) and its descent velocity was noticeably lower than that of the sediment [Figure 6 (*c*)]. As seen in Figure 6 (*d*), the entrained fluid took two to three times longer to reach the bottom of the tank than the particles. Further lateral growth of the entrained fluid at this stage was not apparent. Note that the present measurements did not provide much information on the fine details of the dye field structure. Such fine scale structure of the dye motion after phase separation can result from continuous turbulence generation, or simply the residue motion of earlier time, but the present experimental resolution was not sufficient to resolve these issues, their primary objective being to provide bulk characteristics of both phases of the sediment cloud. Future investigation of fine details of a two-phase sediment cloud would be worthwhile.

4.3 Results and analysis

The LIF images and videos were post-processed to obtain the characteristics (frontal position and half-width) of the entrained fluid and the sediment cloud. For the images captured by the two CCD cameras, the two phases were captured by separate cameras fitted with appropriate filters, giving two sets of images for a single experiment. The resolution was higher than the video camera but limited by the field of view of the CCD cameras. The videos were subsequently converted to a series of color images at 30 Hz frequency. By extracting different color bands in the images, the entrained fluid and sediment cloud were isolated from each other and their characteristics could be quantified separately. The video had the advantage of a larger field of view covering the whole descent process of the sediment cloud, but with lower image resolution. In both the LIF images and videos, the boundary of the entrained fluid and particles were extracted using the Otsu's (1979) method. This method binarizes the grey level image by using all possible pixel value thresholds (background taken as 0, foreground taken as 1), and selects an optimized threshold based on minimizing the spread of pixel values (about the mean of the background and foreground) for each side of the threshold.

4.3.1 Virtual origin and entrainment coefficient

Using the data from the CCD cameras, for each time instant at which measurements were made, r_s, z_s were obtained and N_c was derived. The entrainment coefficient of the sediment cloud as a function of the cloud number is given in Figure 7. Best fit curve of the data was found to be $\alpha = 0.53(1-0.65\,N_c^{\,0.36})$, i.e. $\alpha_o = 0.53$, $c_1 = 0.65$, c_2=0.36 ; this was adopted in the model (in the thermal regime) for all comparisons with experiments. The virtual origin was assumed to be at r_c/α_o in the model prediction of all subsequent comparisons (assumed to be zero if r_c is not reported in studies to be compared). It was also necessary to obtain the entrainment coefficient of the entrained fluid after all sediment particles had fallen out. Using the data in the range of $z > 3l_{ts}$, we found the entrainment coefficient to be 0.07 (average of size A, B and D) and this was adopted in the model in the dispersive regime. Note that if an integral model is to be utilized, a second virtual origin is needed for the sediment cloud in the dispersive regime. The present model circumvents such need.

5 Comparison of model predictions with experiments

5.1 Shape and size of entrained fluid and sediment clouds

The data from the video camera were used in observing the shape and size changes of a sediment cloud during its whole descent process. The predicted shape and size of a sediment cloud at different times are represented as a group of circles (each of them is a computational particle) shown in Figure 8(*a*) for particle size B. At t = 1.3 s, the particles were concentrated at the bottom of the thermal as a thin layer. From t = 3.3 s - 6.6 s, the sediment cloud rained out as a bowl shaped swarm, and its shape elongated in the z-direction as it descended. Finally, the sediment cloud reached the tank bottom, but the entrained fluid continued to descend at a slower rate than the particles and kept on decelerating, reaching only half of the water depth after 13.3 s. The experimental results in Figure 8 (*b*) showed similar results. The predicted and observed behaviors for the other particle sizes were similar except that the thermal-dispersive regime transition occurred at different depths depending on l_{td}. Note that in our model, the dye or the tracer transport is implicitly assumed to be equivalent to the vorticity transport. In general, the transport of the tracer and vorticity is different, but our experimental study of single-phase thermal shows that the size indicated by the tracer is close to that of the vorticity (Zhao et al., submitted), and it is a reasonable approximation for the purpose of our model.

More quantitative comparison of the sediment cloud shape is given in Figure 9 using data of particle size A, B and D. Figure 9(a) shows the predicted and observed circularity of the sediment cloud is defined as 4π times the area of the sediment cloud divided by the square of its perimeter. This can be obtained experimentally with the sediment cloud boundary defined by the Otsu's method. The small scales in the images were filtered off by a median filter. With the outline of sediment cloud obtained, the boundary is carefully tracked manually and the area and circumference of the shape defined by the boundary was computed. The trailing stem portion was not included. To define the boundary of the sediment cloud in the model, two runs were made. The first was based on a single particle diameter for a given particle class, and the other used the upper and lower bound diameters of a particle type (Table 1) in a single run with a bi-disperse population of particles. The lower size limit with smallest w_s defined the upper boundary, and the upper size limit defined the lower boundary. Experimental observation in Figure 9 (a) shows that initially the sediment cloud was somewhat 'less circular' (since sediments concentrated at the bottom of a thermal), and it kept increasing until about $z/l_{t-s} = 7$ (forming a swarm which elongates vertically), and then leveled off and dropped beyond $z/l_{t-s} = 15$.

Some more insights can be obtained by considering the aspect ratio of the sediment cloud. We define the cloud aspect ratio defined as $(z_s - z_{sc})/r_s$, where z_{sc} is the centroid of the sediment cloud. Ruggaber (2000)'s method of obtaining the centroid of a sediment cloud is used. The horizontal center of mass is determined by dividing the mean displacement in the horizontal direction by the cross-sectional area. The vertical center of mass is then determined by dividing the first spatial moment about the horizontal center of mass by the cloud volume (refer to Ruggaber 2000 for details). The centroid is obtained in the model by finding the mean z-position of all computational particles. Figure 9(b) shows the predicted and observed sediment cloud aspect ratio. Experimentally it can be seen the aspect ratio kept increasing, showing the elongation in the vertical direction was faster than the horizontal direction. The sediment cloud was at first a ‘flat ellipsoid’, it then becomes close to a circle, and finally became a ‘tall ellipsoid’. This also explained the leveling off (which is expected to decrease if the cloud descends further) of the cloud circularity beyond $z/l_{t\text{-}s} = 15$.

Despite the fact that both the circularity and aspect ratio are sensitive to the flow details, our simple model is able to predict the trend of both the circularity (Figure 9a) and aspect ratio (Figure 9b) in general. The model predictions are obtained by averaging the predictions for the three particle sizes. Quantitatively comparison shows that the predicted shape is more ‘flattened’ before $z/l_{t\text{-}s} = 10$, and more ‘elongated’ beyond $z/l_{t\text{-}s} = 15$. The irregular predicted trend for $z/l_{t\text{-}s}$ smaller than 5 on both figures shows that the initial uniform distribution of particles is undergoing changes to form a vortex ring structure. If only a single (median) size from a particle type is used, the agreement can be seen to be poorer for both the circularity and aspect ratio, showing that the particle distribution plays an important role in determining the shape of the swarm.

Figure 10 shows the boundary of the sediment cloud and entrained fluid for all 10 experiments (from the video camera) of particle size B at $t = 3.3$ s. Note that the sediment cloud characteristics varied somewhat among runs. Five runs from the CCD cameras in each of the upper and lower regions were used for averaging in the subsequent comparisons.

5.2 Depth and half-width

The predicted penetration depth over time of both the sediment cloud and entrained fluid is compared with observation in Figure 11. Figure 11 (*a*) shows that the predicted sediment cloud penetration depth over time is in reasonable agreement with observation from the thermal to dispersive regime for all particle sizes tested. Only limited data were available for large size particles as they settled to the bottom quickly. There is a slight under-prediction of the descent speed for particle sizes B and D, which can be explained by the fact that the frontal sediment cloud position is governed more by the largest particle size within the range. The penetration depth of the entrained fluid over time is also well predicted as shown in Figure 11 (*b*). Also shown in the figure (dashed line) are the predictions if constant buoyancy is assumed throughout the flow. It can be seen that if the reduction of buoyancy is not accounted for, the cloud descent velocity can be significantly over-predicted for the entrained fluid.

The comparison of the predicted half-wdith of the sediment cloud (from the integral model) and entrained fluid with observation is given in Figure 12. The half-width is defined as half of the maximum width in the *r*-direction. The predictions for sediment cloud half-width are in good agreement with observations as shown in Figure 12 (*a*). Figure 12 (*b*) shows that the predicted entrained fluid half-widths are also in good agreement with observation. This is despite the fact that the model approximates the entrained fluid as a sphere while in reality it is more like an ellipsoid. Again, the dashed line shows the predictions if constant buoyancy is assumed throughout, which can be seen to over-predict the entrained fluid width in all cases.

5.3 The spread of a puff – fluid phase after phase separation

It is noted that the growth rate of the entrained fluid (which can be considered as a vortex ring) in the dispersive regime, is considerably higher than that of a vortex ring (Maxworthy 1974) which has a typical $\alpha \approx 0.01$. It appears that the characteristics of a vortex ring can be affected by the generating mechanism. The shape of the puff observed in our experiments appeared to be somewhat thicker than that of Maxworthy (1974), and a direct comparison of parameters obtained experimentally may not be suitable. The lack of other independent experimental data on the growth rate of the entrained fluid after phase separation prevented a more conclusive remark. For modeling purposes, the use of $\alpha \approx 0.07$ found in this study can be applied to the entrained fluid (in the dispersive regime) for a wide range of sediment cloud release conditions.

6 Comparison with previous studies

The sediment cloud characteristics predicted by the model are compared with representative studies in the literature to show the generality of the model. Comparisons are first made with studies that focused on the thermal regime of sediment clouds, followed by studies on the dispersive regime, and finally studies on the two-phase characteristics of sediment clouds. Virtual origins in these previous studies were typically not specified, and are taken to be zero in the model predictions.

6.1 Thermal regime of sediment clouds

The thermal regime of a sediment cloud was studied by Rahimipour and Wilkinson (1992). Experiments were conducted with graded sand particles of d =

0.150 - 0.350 mm. Initial volume ranged between 3.45 - 7.65 cm^3, giving a total mass of 9.0 - 20.0 g, assuming a typical sand density of 2.6 g/cm^3.

The average size of the graded sand was used for each case assuming a uniform sand size distribution (by size). The settling velocity (required in computing N_c) was computed using the Dietrich's formula (1982). Figure 13 (*a*) shows the predicted ratio between the cloud front velocity and the corresponding miscible thermal velocity, with equal buoyancy at the source as a function of N_c. The prediction is an average curve over 5 runs of four release conditions (each of them collapsing into approximately a single curve). The thermal velocity was taken as $w_{thermal} = 2.3(\sqrt{B_o / \rho_a}) / z_s$ (Scorer 1957). In agreement with the experimental data, the prediction shows that when $N_c<1$, $w_p \approx w_{thermal}$; and when $N_c>1$, then $w_p >> w_{thermal}$ (where w_p is the sediment cloud front velocity) - i.e. the theory's treatment of the sediment cloud as a thermal of constant buoyancy is no longer applicable.

Figure 13 (*b*) shows the predicted and observed growth rate of a sediment cloud in the experiments of Rahimipour and Wilkinson. For $N_c<1$, the growth rate varies slightly ($\alpha \approx 0.2 - 0.3$). For $N_c>1$, the cloud's growth rate reduces drastically indicating the beginning of the dispersive regime. The predicted sediment cloud growth rate in the dispersive regime using a random walk model is also in good agreement with the experimental data.

6.2 Dispersive regime of sediment clouds

The dispersive regime of sediment clouds was studied in detail by Buhler and Papantoniou (1991,1999, 2001), who conducted sediment cloud experiments used

d = 1.95 mm (Buhler and Papantoniou 1991) and d = 2.62 mm (Buhler and Papantoniou 1999), and measured average w_s = 18.8 and 21.8 cm/s respectively. For consistency, the settling velocity was computed using the Dietrich's formula (1982) in the model. The particle density was 2.6 g/cm^3. Selected experimental results from their studies are compared with our model predictions.

A length scale z_o similar to the cloud number was defined to normalize the length dimension:

$$z_o = (\frac{B_o}{\rho_a})^{1/2} / w_s$$

Figure 14 (*a*) shows the comparison of the predicted sediment cloud widths with observation. The prediction curve is obtained by averaging the predicted velocity of the four cases, each of which is an average of 5 runs. It appears that the model slightly over-predicts the growth of the cloud on average. Using the lower measured w_s improves the results (the measured settling velocity exhibits some degree of variation), but would be unnecessary given the fact that other factors may also contribute to the deviation, such as the position of the virtual origin. Overall, the predictions appear to be still within the observed range.

Figure 14 (*b*) shows the comparison of the predicted and observed descent velocities. Both the prediction and observation show that w_p is higher than the individual particle settling velocity, by a factor of 1.1 - 1.7. The prediction slightly under predicts the velocity, possibly for the same reasons that pertain to the cloud width.

6.3 Two-phase characteristics measurements of sediment clouds

Luketina and Wilkinson (1998) carried out experiments that provided an initial understanding of the two-phase characteristics of a sediment cloud. Here, 6 g of glass beads (assumed density 2.5 g/cm^3) of d = 0.4 mm with w_s= 6.5 cm/s was released from rest into a stagnant ambient. The settling velocity was computed using the Dietrich's formula (1982). The descent process of both the particle and entrain fluid descent position with time were video recorded. Figure 15 shows that the predicted (obtained by averaging 5 simulations) descent position for the sediment cloud is in good agreement with observation. The agreement is also good for the entrained fluid considering the variability for the entrained fluid after phase separation. Similar comments can be made for the comparison of predictions against recent experiments of Duguen et al. (2011). These experiments were conducted in a spherical container (Figure 16), with data deduced from the published time series of photographs (0.5 g of particles with density 2.6 g/cm^3; d=0.603 mm; w_s computed by the Dietrich's formula).

6.4 Particle size effect on spreading rate

Gensheimer et al. (2013) reported that the spread rate of a sediment cloud in the thermal regime at a given depth increases with decreasing particle size. This can in fact be reflected in the variable α formula used in this study (α = 0.53 (1-0.65 $Nc^{0.36}$)). Figure 17 shows the sediment cloud growth observed by Gensheimer et al. (2013) with particle size A:0.725 mm, and AE: 0.120 mm. It is evident that the spread rate of particle size AE is greater than that of A. The prediction by using a variable α can be seen to be consistent with this observation.

7 Conclusions

The mixing characteristics of a two-phase sediment cloud were investigated experimentally and theoretically in this study. We report the first systematic experimental programme to quantify the characteristics of both the fluid phase and the solid phase of such sediment clouds. Experimental observation showed that initially the particle cloud forms a thermal-like flow and is transported with the entrained fluid. With time, the particles separate from the entrained fluid when the cloud velocity decreases to approximately the particle setting velocity. Subsequently, the particle cloud descends as a bowl-shaped swarm, and the entrained fluid descends as a puff-like flow.

Theoretically, Turner (1964)’s expanding Hill’s vortex model has been shown for the first time to satisfy the volume conservation equation by suitably modifying the characteristic width of the sphere. The entrainment pattern and internal structure predicted by the expanding Hill’s vortex with a specified entrainment coefficient was also studied and shown to be physically realistic when compared with that of a non-entraining vortex ring, and an entraining thermal. Subsequently, we extend the Turner’s model and propose a two-phase model for a sediment cloud. The model predicts the characteristics of both the fluid and solid phases covering both the thermal and dispersive regimes. The entrained fluid characteristics are solved by an integral model accounting for the buoyancy loss (due to particle separation) in each time step. The flow field induced by the sediment thermal is approximated by an expanding Hill's vortex centered at the centroid and with the size of the entrained fluid. The particle equation of motion under the effect of the induced flow is solved for each computational particle. A random walk model using a hydrodynamic diffusion coefficient accounts for the random fluctuation of particles in the dispersive regime.

The model predictions are compared with a wide range of experimental data of the two-phase mixing characteristics of a sediment cloud. The predicted transient descent depth and half-width, and descent velocity of a sediment cloud and its entrained fluid, are in good agreement with observation. The time-varying shape of a sediment cloud over time, which is highly sensitive to flow details, can also be reasonably predicted. Certain model approximations and assumptions have limited our ability to predict the finer details of the flow, but the good agreement between predictions and observations in key sediment cloud characteristics indicates that we have captured the important physics of the problem. The model is computationally much more efficient than a two-phase computational fluid dynamics model, and at the same time gives more detail than traditional integral models. The simplicity of the model also permits possible extensions to consider other problems frequently encountered in practice, e.g., multiple particle size releases, or the effects of an ambient current. These will be subjects for future study.

Acknowledgements

This research was supported by the National Research Foundation Singapore through the Singapore-MIT Alliance for Research and Technology's CENSAM IRG research programme. We also acknowledge the anonymous reviewers for the comments and suggestions made which have improved the manuscript.

Appendix A Hill's vortex induced velocities and their derivatives

This appendix presents the derivation of the derivatives of velocities presented in the main text.

For a Hill's vortex translating at speed U with radius a centered at (z_c, 0), the vortex induced velocity field to a stationary observer is given by:

Inside the entrained fluid ($R<a$):

$$u_z = -\frac{3U}{4}[4(\frac{r}{a})^2 + 2(\frac{z-z_c-Ut}{a})^2 - \frac{10}{3}] \qquad \text{(A.1)}$$

$$u_r = \frac{3U}{2a^2} r(z-z_c-Ut) \qquad \text{(A.2)}$$

Outside the entrained fluid ($R>a$):

$$u_z = \frac{Ua^3}{2}\frac{2(z-z_c-Ut)^2 - r^2}{[(z-z_c-Ut)^2 + r^2]^{5/2}} \qquad \text{(A.3)}$$

$$u_r = \frac{3Ua^3 r(z-z_c-Ut)}{2[(z-z_c-Ut)^2 + r^2]^{5/2}} \qquad \text{(A.4)}$$

The convective derivatives of the velocity field are needed to evaluate the forces acting on each computational particle:

$$\frac{Du_z}{Dt} = \frac{\partial u_z}{\partial t} + (\frac{\partial u_z}{\partial z} + \frac{\partial u_r}{\partial r} + \frac{u_r}{r})u_z$$

$$\frac{Du_r}{Dt} = \frac{\partial u_r}{\partial t} + (\frac{\partial u_z}{\partial z} + \frac{\partial u_r}{\partial r} + \frac{u_r}{r})u_r$$

Partial derivatives presented in the above equations can be evaluated as follow:

Inside the entrained fluid ($R<a$):

$$\frac{\partial u_z}{\partial z} = -\frac{3U(z - z_c - Ut)}{a^2} \qquad \text{(A.5)}$$

$$\frac{\partial u_z}{\partial t} = \frac{3U^2}{a^2}(z - z_c - Ut) \qquad \text{(A.6)}$$

$$\frac{\partial u_r}{\partial r} = \frac{3U(z - z_c - Ut)}{2a^2} \qquad \text{(A.7)}$$

$$\frac{\partial u_r}{\partial t} = -\frac{3U^2}{2a^2} r \qquad \text{(A8)}$$

Outside the entrained fluid ($R>a$):

$$\frac{\partial u_z}{\partial z} = -\frac{3Ua^3}{2}\frac{(z - z_c - Ut)[2(z - z_c - Ut)^2 - 3r^2]}{[(z - z_c - Ut)^2 + r^2]^{7/2}} \qquad \text{(A.9)}$$

$$\frac{\partial u_z}{\partial t} = \frac{3U^2a^3}{2}\frac{(z - z_c - Ut)[2(z - z_c - Ut)^2 - 3r^2]}{[(z - z_c - Ut)^2 + r^2]^{7/2}} \qquad \text{(A.10)}$$

$$\frac{\partial u_r}{\partial r} = \frac{3Ua^3}{2}\frac{(z - z_c - Ut)[2(z - z_c - Ut)^2 - 4r^2]}{[(z - z_c - Ut)^2 + r^2]^{7/2}} \qquad \text{(A.11)}$$

$$\frac{\partial u_r}{\partial t} = \frac{3U^2a^3}{2}\frac{r[4(z - z_c - Ut)^2 - r^2]}{[(z - z_c - Ut)^2 + r^2]^{7/2}} \qquad \text{(A.12)}$$

Note that in the above equations, t is a variable different from the physical time. In every time step, we assume a Hill's vortex centered at (z_c ,0) and radius r_f translating at $U = w_f$. The instantaneous value of the partial derivatives in each of the model time step is given by setting $t \rightarrow 0$. This results in the equations appeared in the main text after accounting for the center position shift.

Appendix B Dietrich's formula (1982) for settling velocity of spherical particles

The Dietrich's formula (1982) used for computing settling velocity of spherical particles (0.01 mm - 100 mm) is given as:

$$\log_{10} w^* = -3.76715 + 1.92944 \log_{10} D^* - 0.09815 (\log_{10} D^*)^2 - 0.00557 (\log_{10} D^*)^3 + 0.00056 (\log_{10} D^*)^4 \quad (B.1)$$

where

$$w^* = \frac{w_s^{\ 3}}{(\rho_p / \rho_a - 1) g \nu}; \quad (B.2)$$

$$D^* = \frac{(\rho_p / \rho_a - 1) g d^3}{\nu^2} \quad (B.3)$$

Appendix C Estimate of the maximum velocity attained by a thermal

We provide in this appendix an order of magnitude estimation of the maximum velocity attained by a thermal. Escudier and Maxworthy (1973) derived the asymptotic solutions of a round thermal in both the initial acceleration and thermal regimes with the following dimensionless variables:

$$\bar{t} = \left(\frac{\alpha g F_o}{r_o}\right)^{1/2} t; \qquad \bar{w} = \left(\frac{\alpha}{r_o F_o g}\right)^{1/2} w \qquad \text{(C.1)}$$

Thus, for the initial acceleration phase:

$$\bar{w} \approx \frac{\bar{t}}{1 + k - F_o} \qquad \text{(C.2)}$$

and for the thermal regime:

$$\bar{w} \approx \frac{\bar{t}^{-1/2}}{2^{3/4}(1+k)^{1/4}} \qquad \text{(C.3)}$$

where $k \approx 0$ is the added mass coefficient; $F_o = \frac{\rho_o - \rho_a}{\rho_a}$ is the excess density ratio.

The maximum velocity of the thermal occurs approximately when *t* of the initial acceleration regime is equal to *t* of the thermal regime. Equating the two results in an equation expressing the velocity at this particular time:

$$w_{\max} = \sqrt{\frac{g r_o (\rho_p - \rho_a) / \rho_a}{2\alpha}} \, \frac{1}{[1 - (\rho_p - \rho_a) / \rho_a]^{1/3}} \qquad \text{(C.4)}$$

where r_o is approximated (sufficient for an order of magnitude estimation) as the radius of an equivalent sphere with the same volume as the particle release mass.

References

1. Batchelor GK (1967) An introduction to fluid dynamics. Cambridge Univeristy Press.

2. Buhler J, Papantoniou DA (1991) Swarms of coarse particles falling through a fluid. In Environmental Hydraulics, Lee and Cheung (eds), Balkema, Rotterdam

3. Buhler J, Papantoniou DA (1999) Barge dumping of rubble in deep water. In Environmental Hydraulics, Lee, Jayawardena and Wang (eds), Balkema, Rotterdam

4. Buhler J, Papantoniou DA (2001) On the motion of suspension thermals and particle swarms. J Hydr Res 39(6): 643-653

5. Bush JWM, Thurber BA, Blanchette F (2003) Particle clouds in homogeneous and stratified environments. J Fluid Mech 489:29-54

6. Crowe CT, Sommerfeld M, Tsuji Y (1998) Multiphase flows with droplets and particles. CRC Press, Boca Raton, Fla.

7. Davis RH, Hassen MA (1988) Spreading of the interface at the top of a slightly polydispersesedimenting suspension. J Fluid Mech 196:107-134

8. Davis RH, Hassen MA (1989) Corrigendum to Spreading of the interface at the top of a slightly polydispersesedimenting suspension. J Fluid Mech 202:598-599

9. Deguen R, Olson P, Cardin P (2011) Experiments on turbulent metal-silicate mixing in a magma ocean. Earth and Planetary Science Letters 310: 303-313

10. Dietrich W (1982) Settling velocity of natural particles. Water Resources Research 18(6):1615-1626

11. Escudier MP, Maxworthy T (1973) On the motion of turbulent thermals. J Fluid Mech 61(3):541-552

12 Gensheimer, R.J., Adams, E.E. and Law, A.W.K. (2013) Dynamics of particle clouds in ambient currents with application to open water sediment disposal. J. Hydraulic Engineering, ASCE 139(2). DOI: 10.1061/(ASCE)HY.1943-7900.0000659

13. Gu J, Li CW (2004) Modeling instantaneous discharge of unsorted particle cloud in ambient water by an Eulerian-Lagrangian method. J Hydr Res: 42(4):399-405

14. Guazzelli E, Hinch J (2011) Fluctuations and instability in sedimentation. Annu Rev Fluid Mech 43:97-116

15. Hill MJM (1894) On a spherical vortex. Philos Trans Roy Soc London Ser A 185:213-245

16. Kitanidis PK (1994) Particle-tracking equations for the solution of the advection-dispersion equation with variable coefficients. Water Resources Research 30(11):3225-3227

17. Lee WY (2010) Mixing of horizontal sediment laden jets. PhD Thesis, Department of Civil Engineering, The University of Hong Kong

18. Li CW (1997) Convection of particle thermals. J Hydr Res 35(3):363-376

19. Luketina D, Wilkinson D (1998) The transition to the swarm phase for a particle cloud. Proc. 13th Australasian Fluid Mechanics Conference, Melbourne, Australia.

20. Maxworthy T (1974) Turbulent vortex rings. J Fluid Mech 64(2): 227-239

21. Morton BR, Taylor GI, Turner JS (1956) Turbulent gravitational convection from maintained and instantaneous sources. Proc R Soc. Lond A 234: 1-23

22. Nicolai H, Herzhaft B, Hinch EJ, Oger L, Guazzelli E (1995) Particle velocity fluctuations and hydrodynamic self-diffusion of sedimenting non-Brownian spheres. Phys. Fluids 7:12–23

23. Noh Y, Fernando HJS (1993) The transition in the sedimentation pattern of a particle cloud. Phys of Fluids A 5(12):3049-3055

24. Otsu N (1979) Threshold selection method from gray-level histograms. IEEE Transactions on Systems Man and Cybernetics 9(1):62-66

25. Pignatel F, Nicolas M, Guazzelli E (2011) A falling cloud of particles at a small but finite Reynolds number. J Fluid Mech 671:34-51

26. Rahimipour H, Wilkinson D (1992) Dynamic behaviour of particle clouds. Proc. 11th Australasian Fluid Mechanics Conference, Hobart, Australia.

27. Ruggaber GJ (2000) The dynamics of particle clouds related to open-water sediment disposal. PhD Thesis, Department of Civil and Environmental Engineering, Massachusetts Institute of Technology

28. Scase MM, Caulfield CP, Linden PF, Dalziel SB (2007) Local implications for self-similar turbulent plume models. J Fluid Mech 575:257-265

29. Scorer RS (1957) Experiments on convection of isolated masses of buoyant fluid. J Fluid Mech 2(6):583-594

30. Swamee PK and Ojha CSP (1991) Drag coefficient and fall velocity of nonspherical particles. J. Hydr. Engrg., ASCE 117(5): 660-667

31. Turner JS (1957) Buoyant vortex ring. Proc. Roy. Soc. Lond. A. 239: 61-75

32. Turner JS (1964) The flow into an expanding spherical vortex. J Fluid Mech 18(2):195-208

33. Turner JS (1973) Buoynacy effects in fluids. Cambridge University Press

34. Zhao B, Law AWK, Adams EE, Shao D, Huang Z (2012) Effect of air release height on the formation of sediment thermals in water. J. Hydraulic Research 50(5): 532-540

35. Zhao B, Law AWK, Lai ACH, Adams EE, (2013) On the internal vorticity and scalar concentration structures of miscible thermals. Submitted to J Fluid Mech.

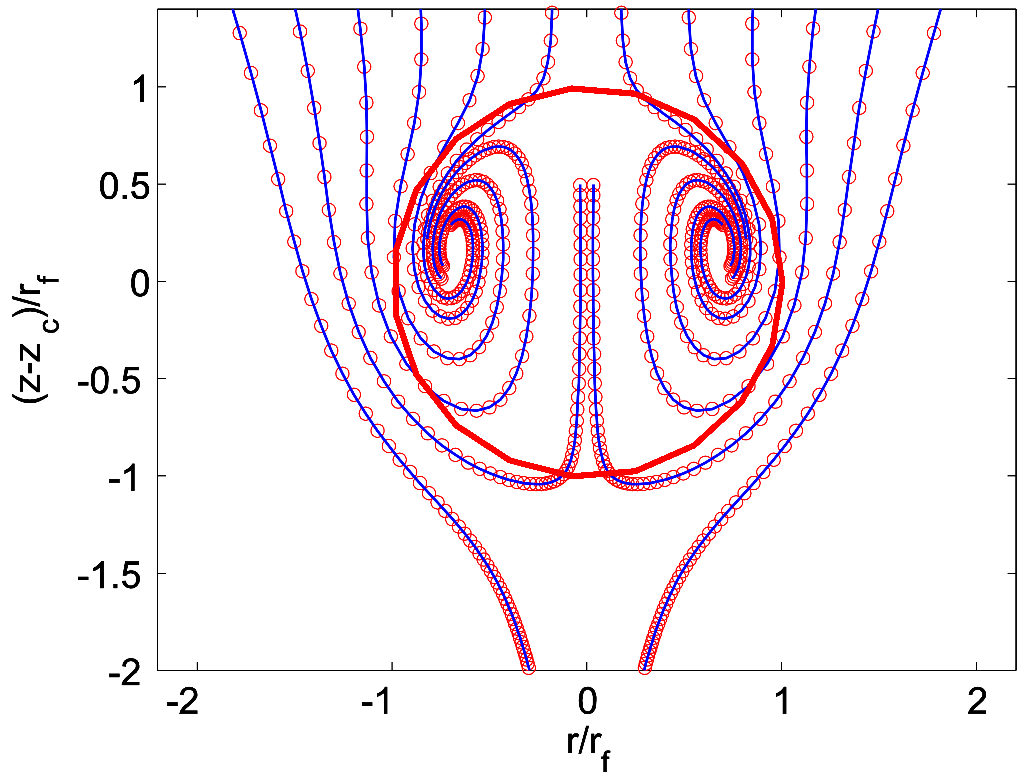

1
0.5
0
-0.5
-1
-1.5
-2
$(z-z_c)/r_f$
-2
-1
0
1
2
r/r_f

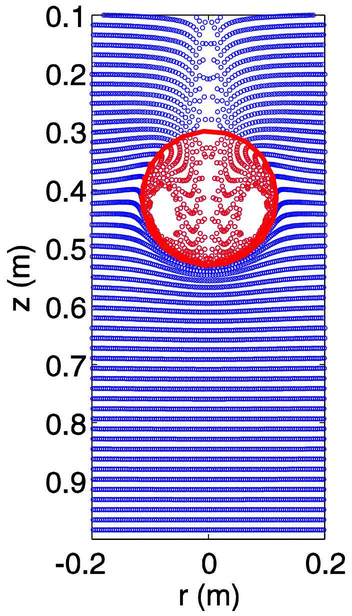

0.1
0.2
0.3
0.4
0.5
0.6
0.7
0.8
0.9
z (m)
-0.2
0
0.2
r (m)

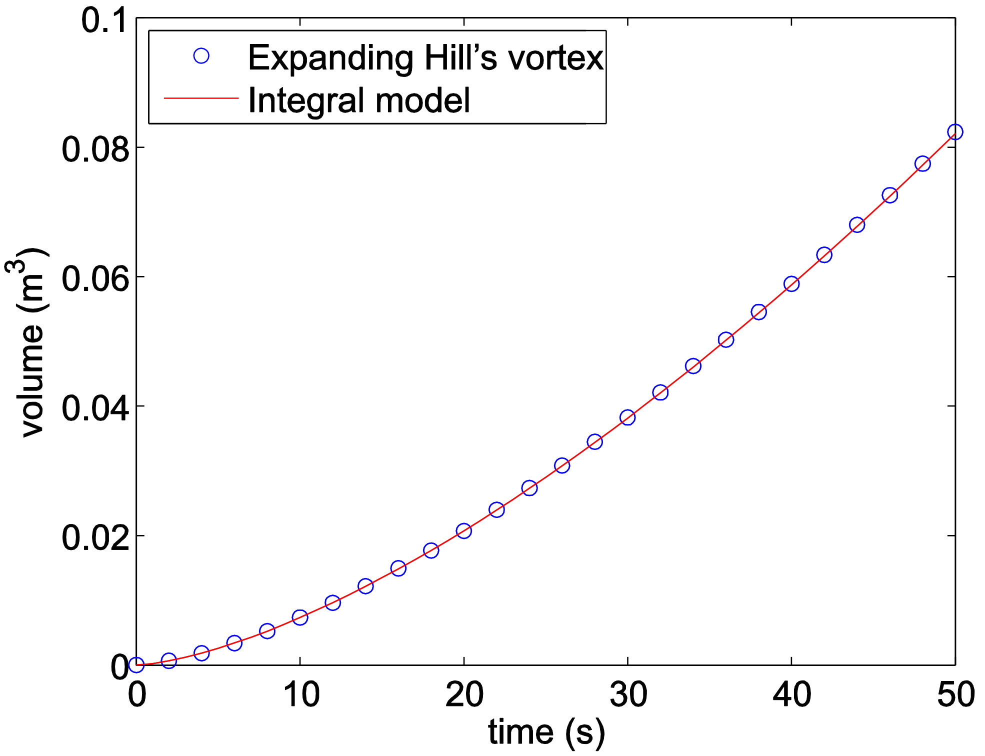
Expanding Hill's vortex
Integral model
volume (m^3)
0.1
0.08
0.06
0.04
0.02
0
0
10
20
30
40
50
time (s)

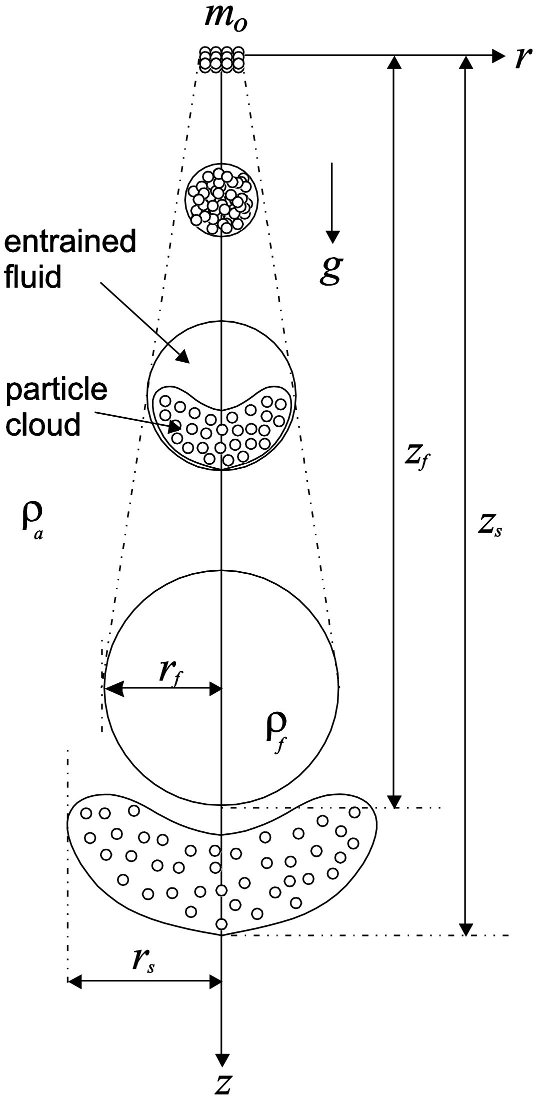
m_o
r
g
entrained fluid
particle cloud
ρ_a
z_f
z_s
r_f
ρ_f
r_s
z

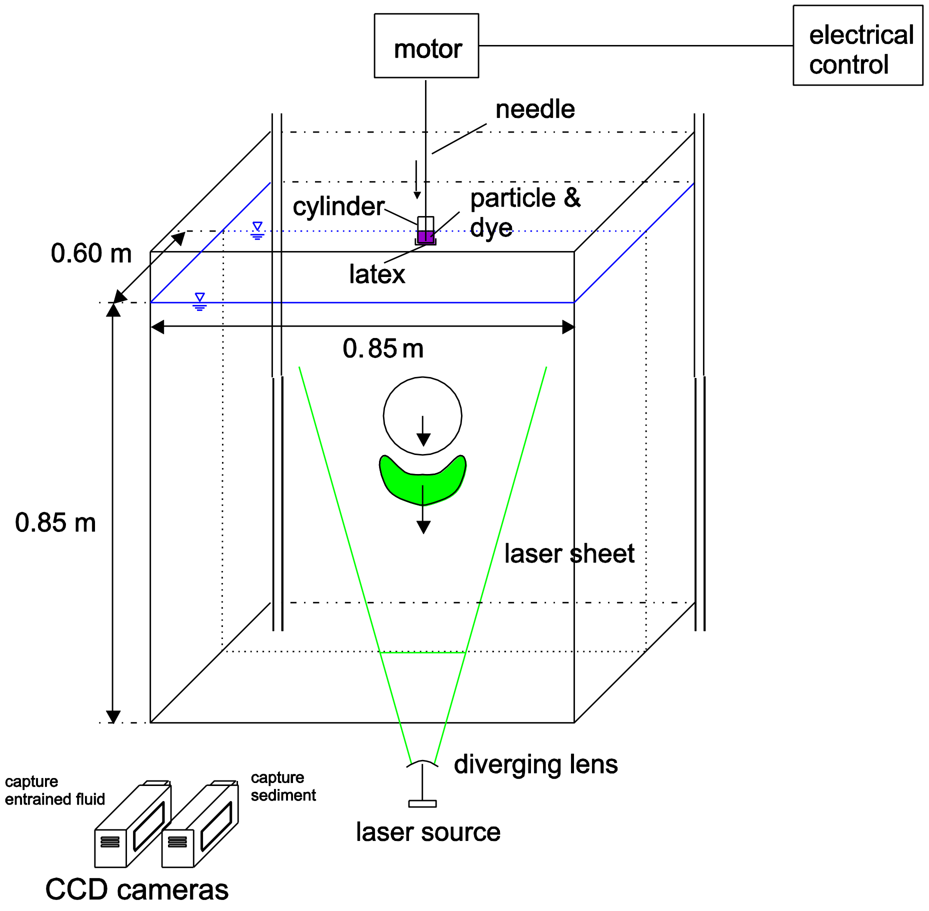
motor
electrical control
needle
cylinder
particle & dye
latex
0.60 m
0.85 m
0.85 m
laser sheet
diverging lens
laser source
capture entrained fluid
capture sediment
CCD cameras

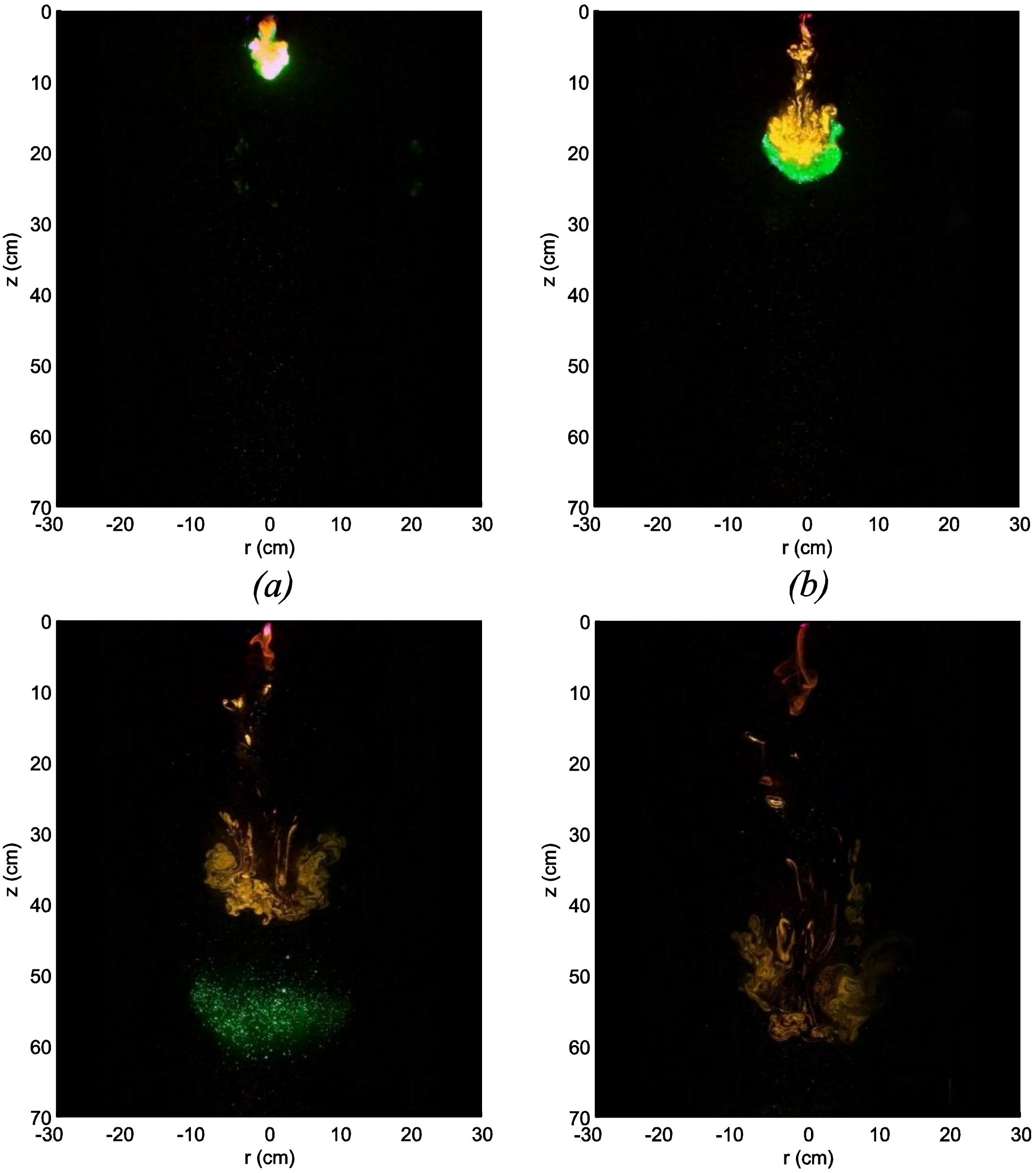
0
10
20
30
40
50
60
70
z (cm)
-30
-20
-10
0
10
20
30
r (cm)

(a)

(b)

(c)

(d)

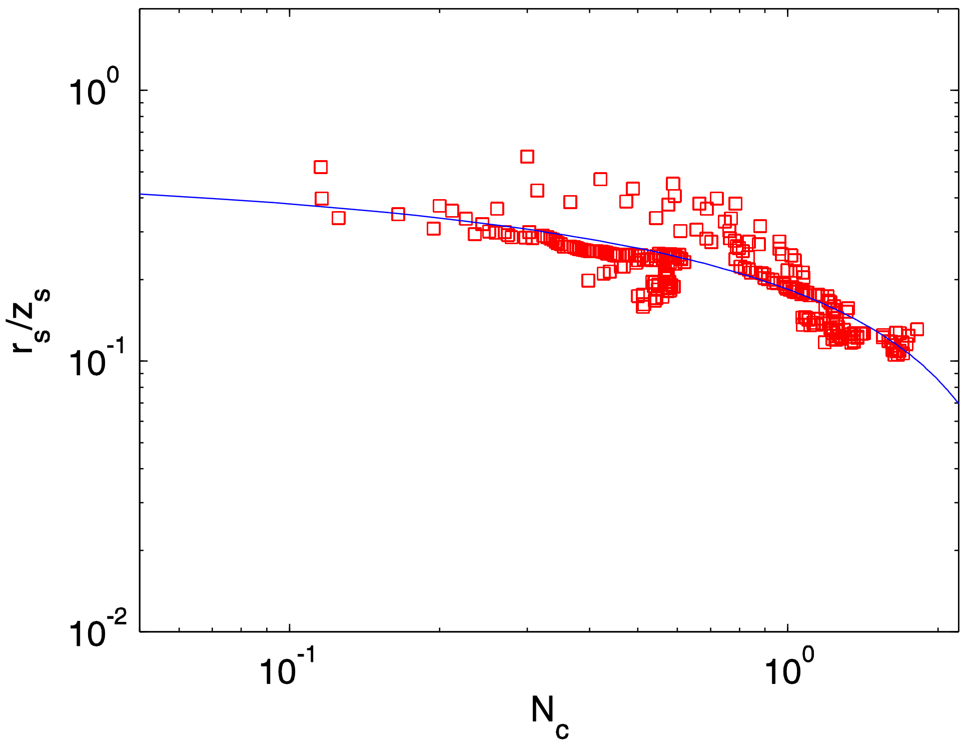

10^0
10^{-1}
10^{-2}
r_s/z_s
10^{-1}
10^0
N_c

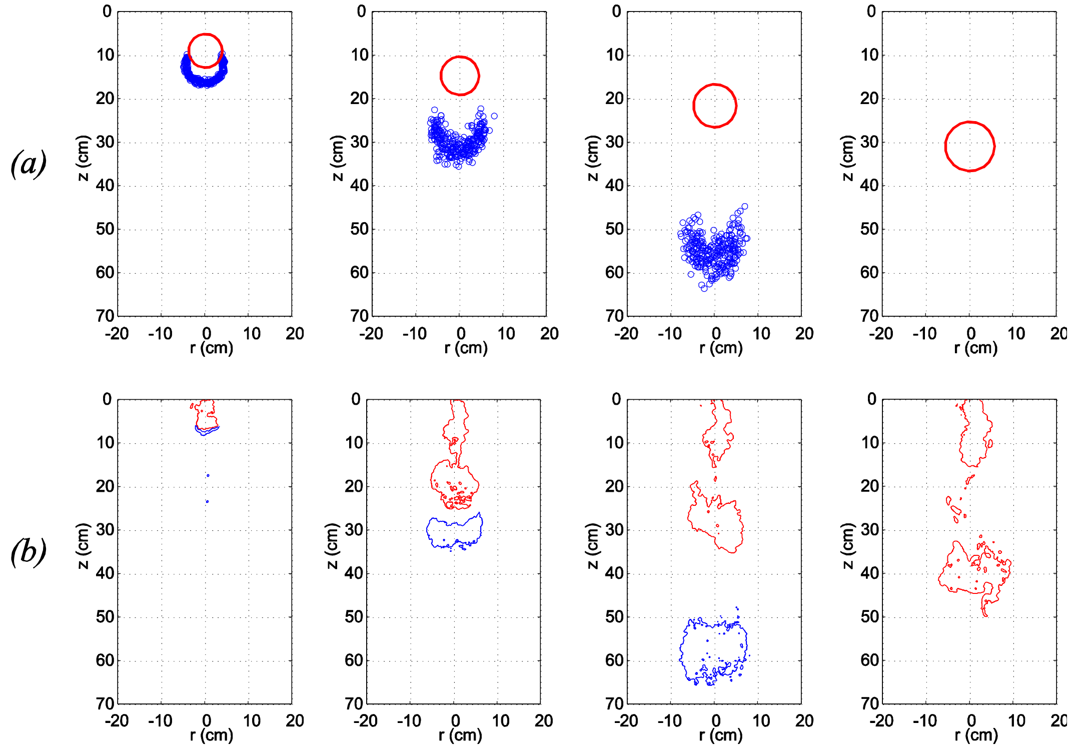

(a)
(b)
z (cm)
r (cm)
0
10
20
30
40
50
60
70
-20
-10
0
10
20

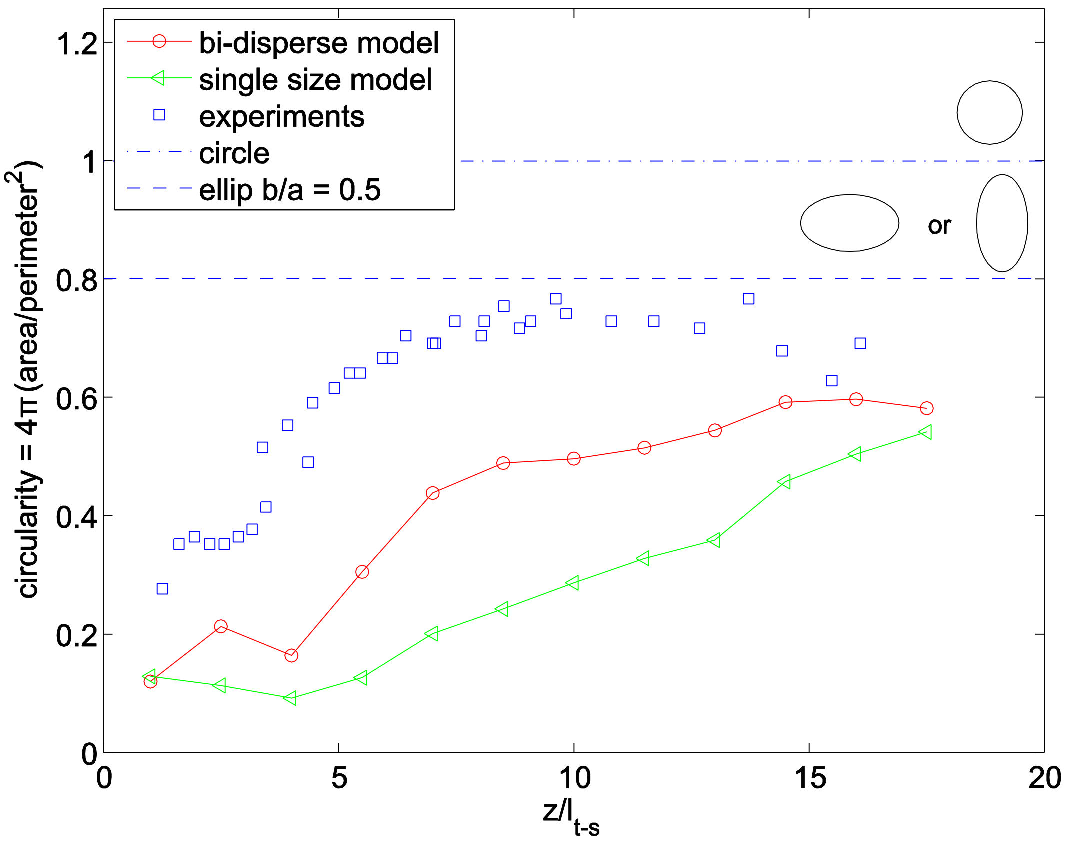
bi-disperse model
single size model
experiments
circle
ellip b/a = 0.5
or
circularity = 4π(area/perimeter^2)
z/l$_{t-s}$
0
0.2
0.4
0.6
0.8
1
1.2
0
5
10
15
20

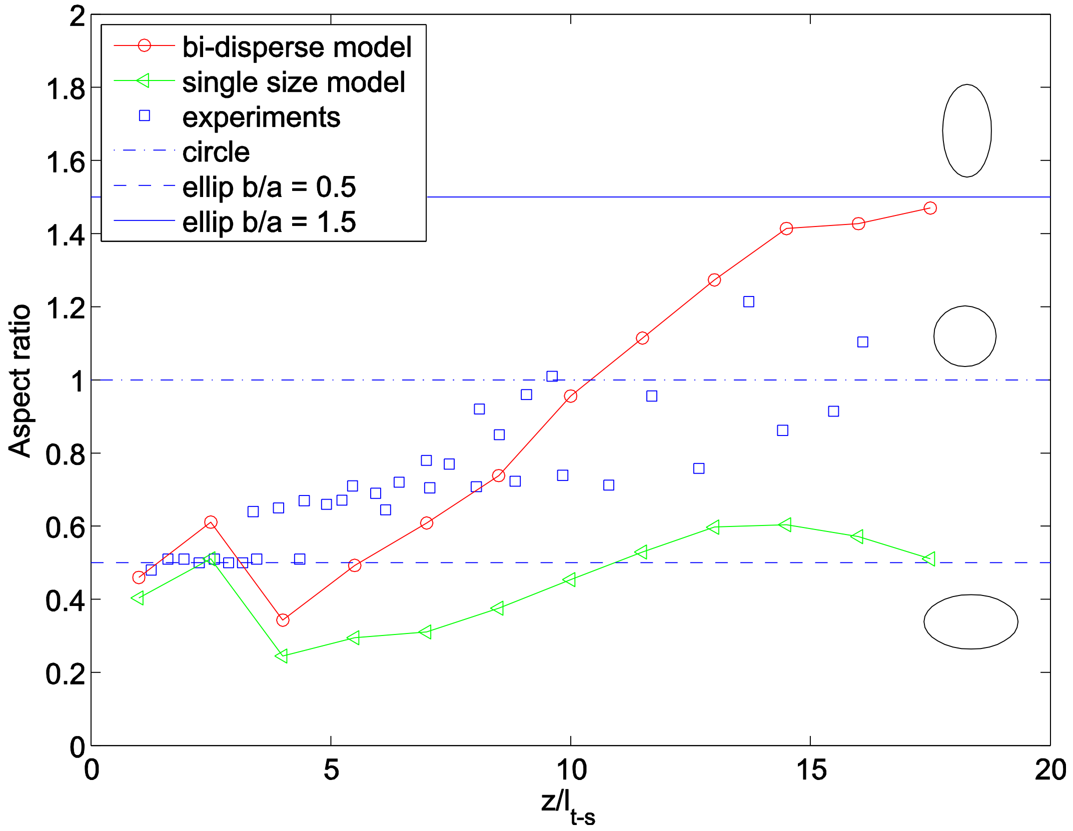
bi-disperse model
single size model
experiments
circle
ellip b/a = 0.5
ellip b/a = 1.5
Aspect ratio
z/l$_{t-s}$
0
0.2
0.4
0.6
0.8
1
1.2
1.4
1.6
1.8
2
0
5
10
15
20

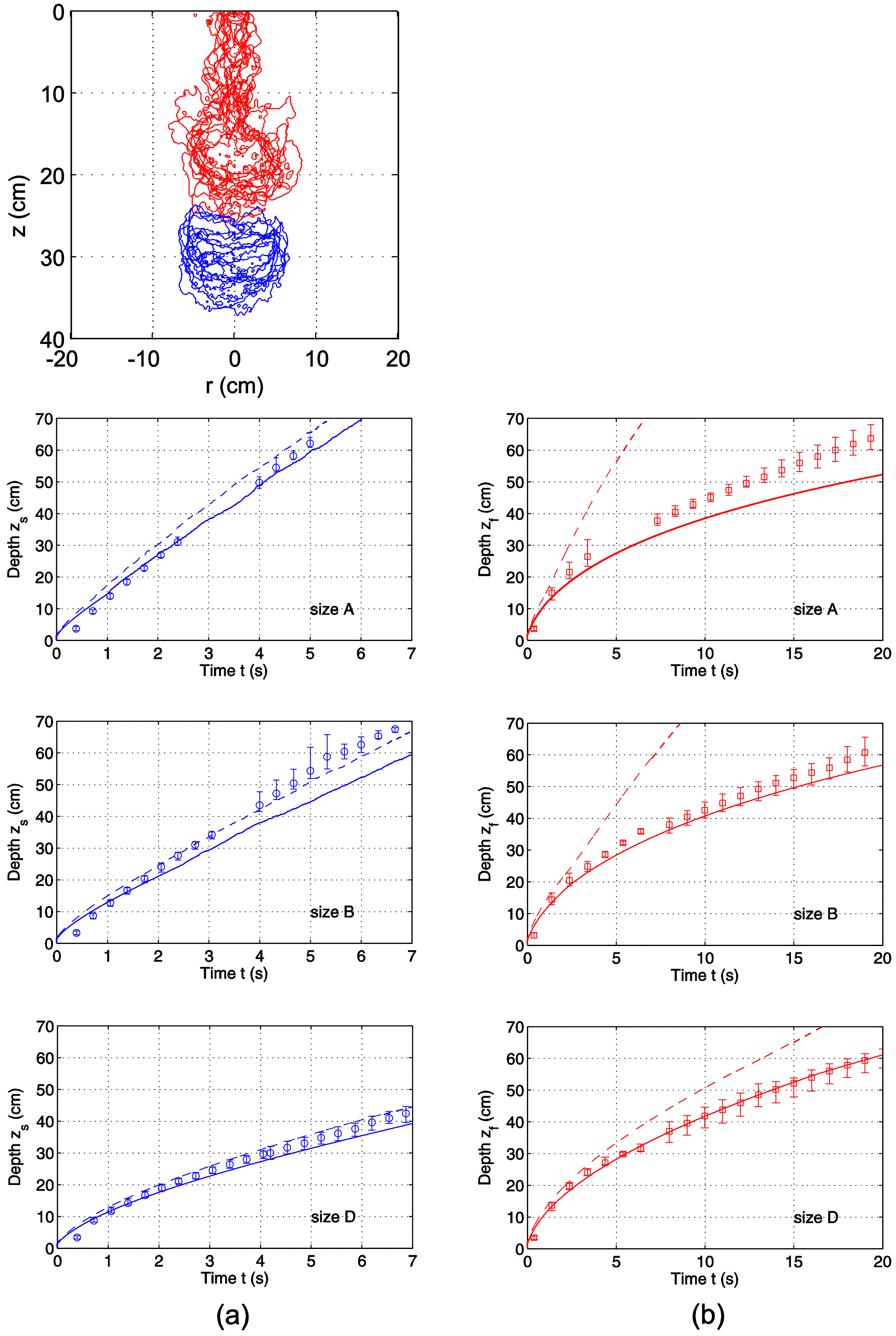
z (cm)
r (cm)
0
10
20
30
40
-20
-10
0
10
20
Depth z_s (cm)
Time t (s)
size A
size B
size D
Depth z_f (cm)
Time t (s)
size A
size B
size D
0
10
20
30
40
50
60
70
0
1
2
3
4
5
6
7
0
5
10
15
20
(a)
(b)

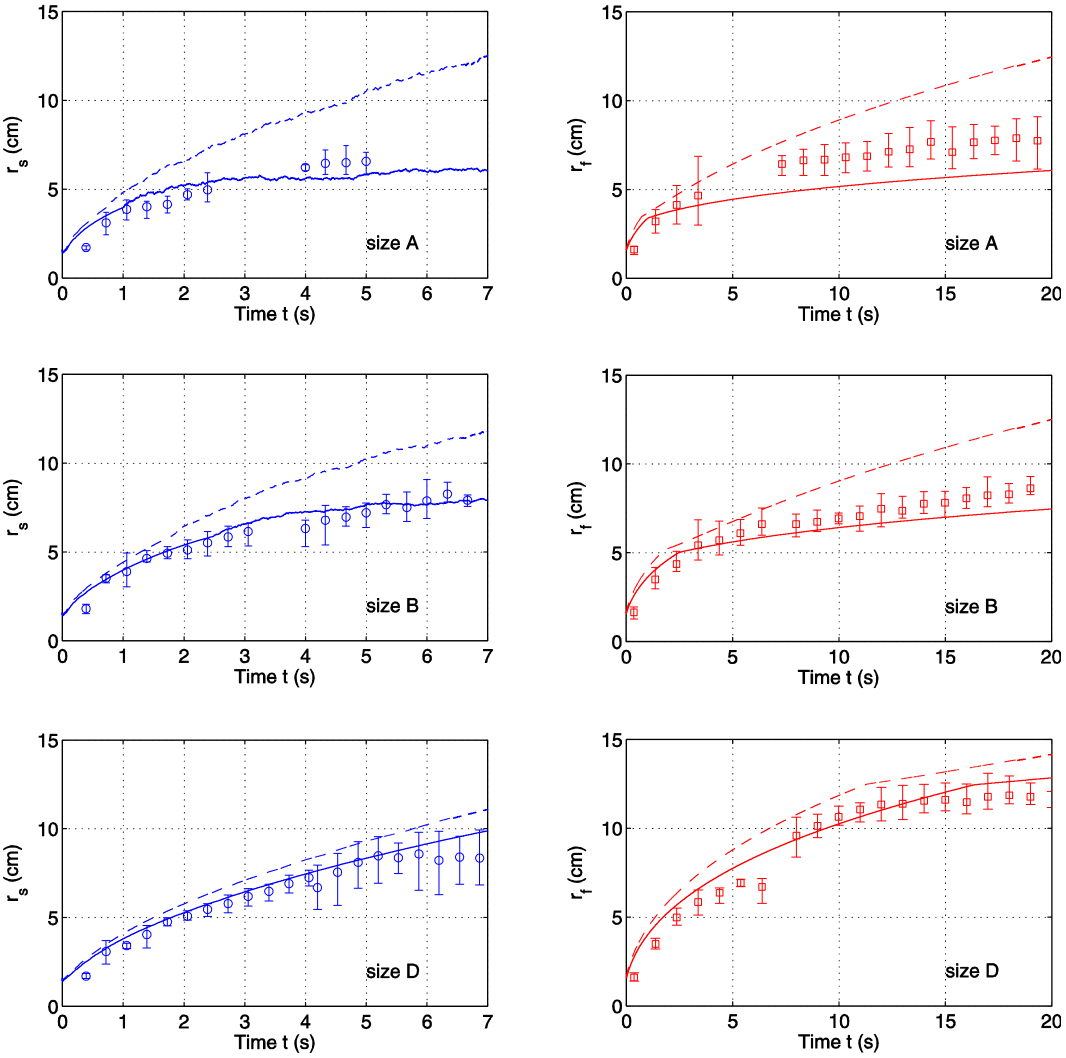

(a)

(b)

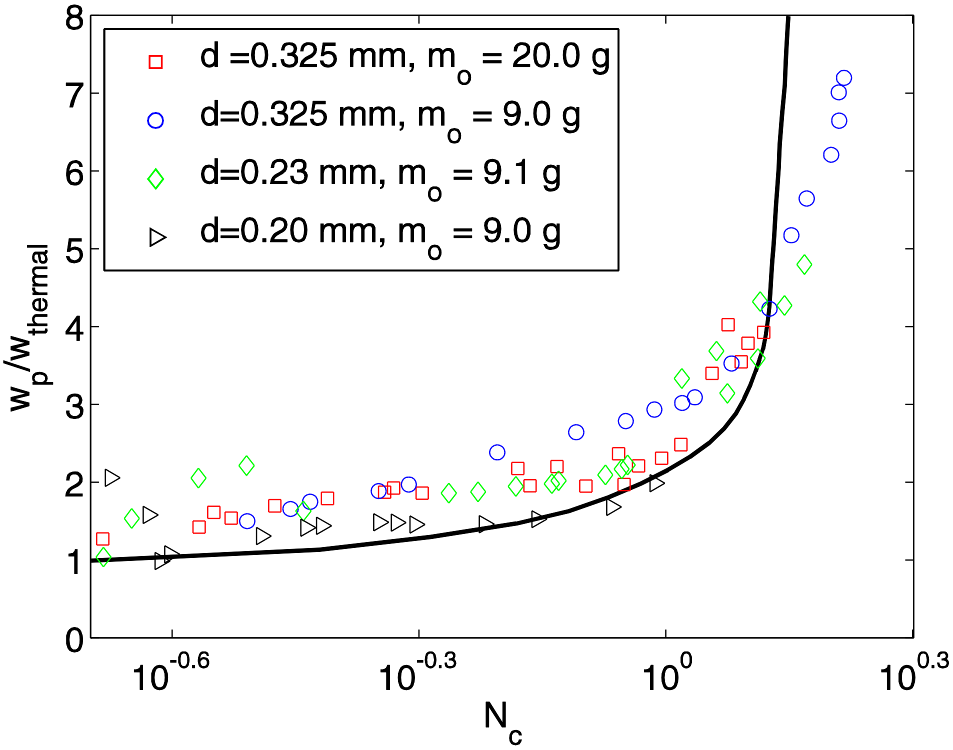
d =0.325 mm, m_o = 20.0 g
d=0.325 mm, m_o = 9.0 g
d=0.23 mm, m_o = 9.1 g
d=0.20 mm, m_o = 9.0 g
$w_p/w_{thermal}$
0
1
2
3
4
5
6
7
8
$10^{-0.6}$
$10^{-0.3}$
10^0
$10^{0.3}$
N_c

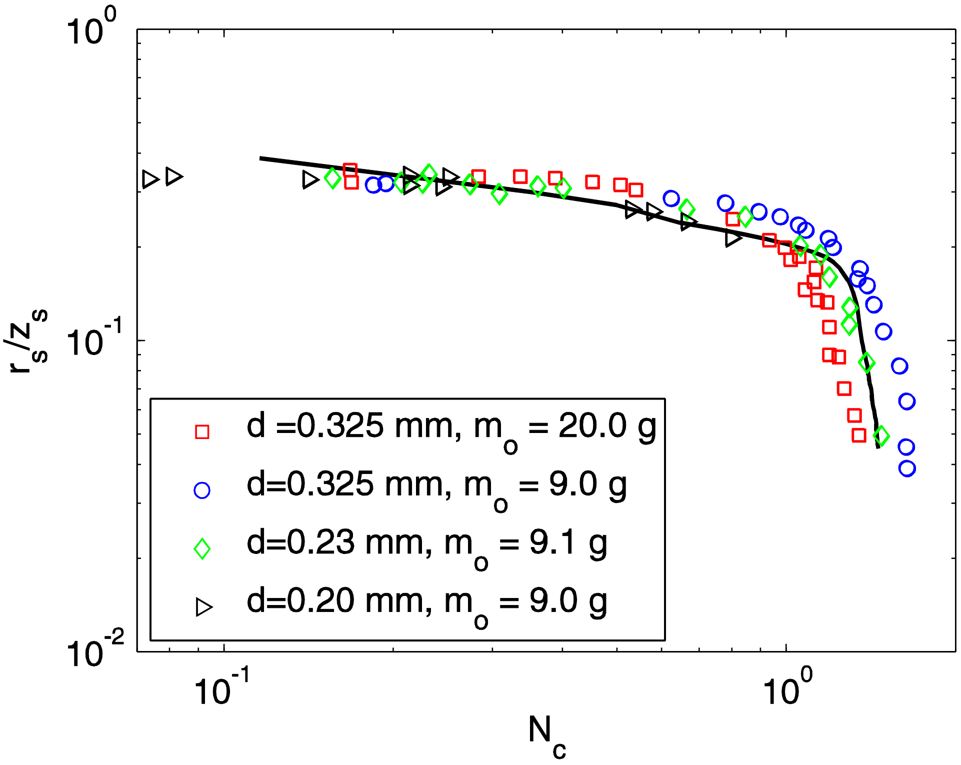
d =0.325 mm, m_o = 20.0 g
d=0.325 mm, m_o = 9.0 g
d=0.23 mm, m_o = 9.1 g
d=0.20 mm, m_o = 9.0 g
r_s/z_s
10^0
10^{-1}
10^{-2}
10^{-1}
10^0
N_c

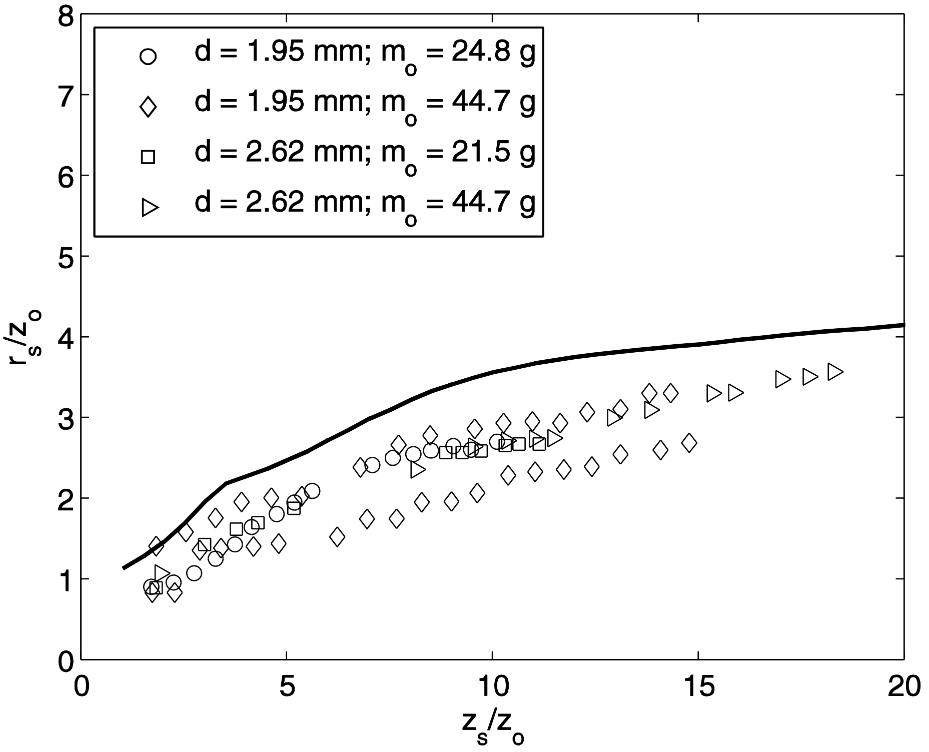
d = 1.95 mm; m_o = 24.8 g
d = 1.95 mm; m_o = 44.7 g
d = 2.62 mm; m_o = 21.5 g
d = 2.62 mm; m_o = 44.7 g
r_s/z_o
z_s/z_o
0
1
2
3
4
5
6
7
8
0
5
10
15
20

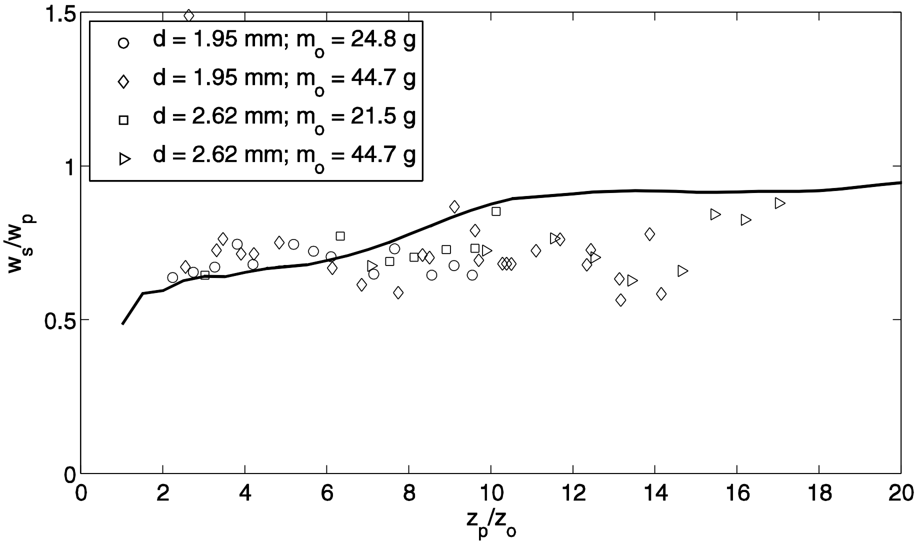
d = 1.95 mm; m_o = 24.8 g
d = 1.95 mm; m_o = 44.7 g
d = 2.62 mm; m_o = 21.5 g
d = 2.62 mm; m_o = 44.7 g
w_s/w_p
z_p/z_o
0
0.5
1
1.5
0
2
4
6
8
10
12
14
16
18
20

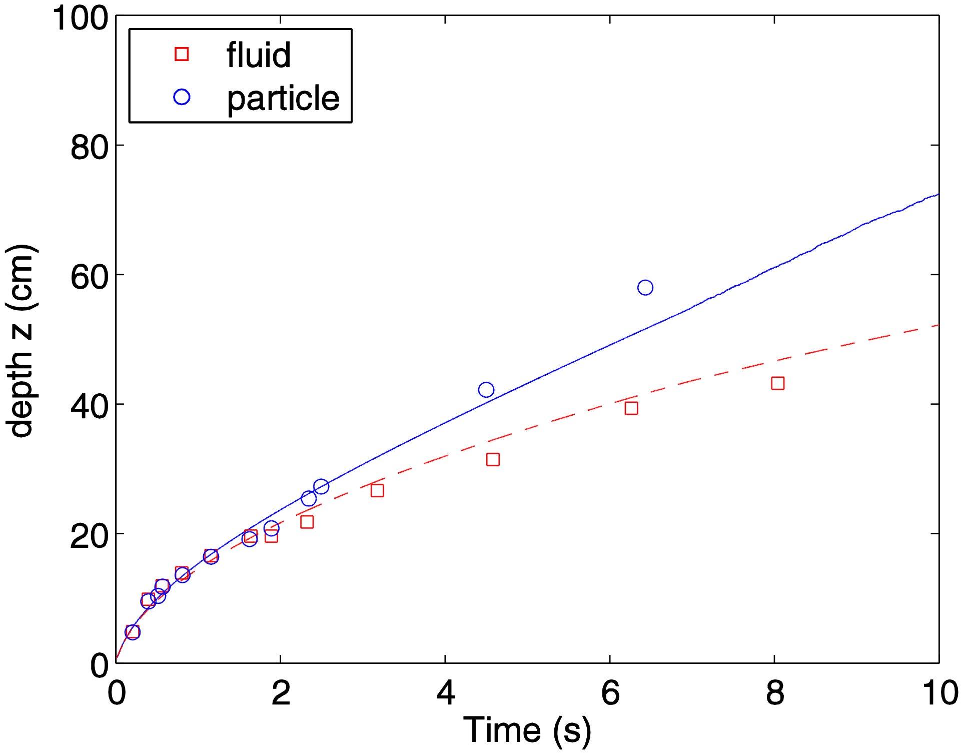
□ fluid
○ particle
depth z (cm)
0
20
40
60
80
100
Time (s)
0
2
4
6
8
10

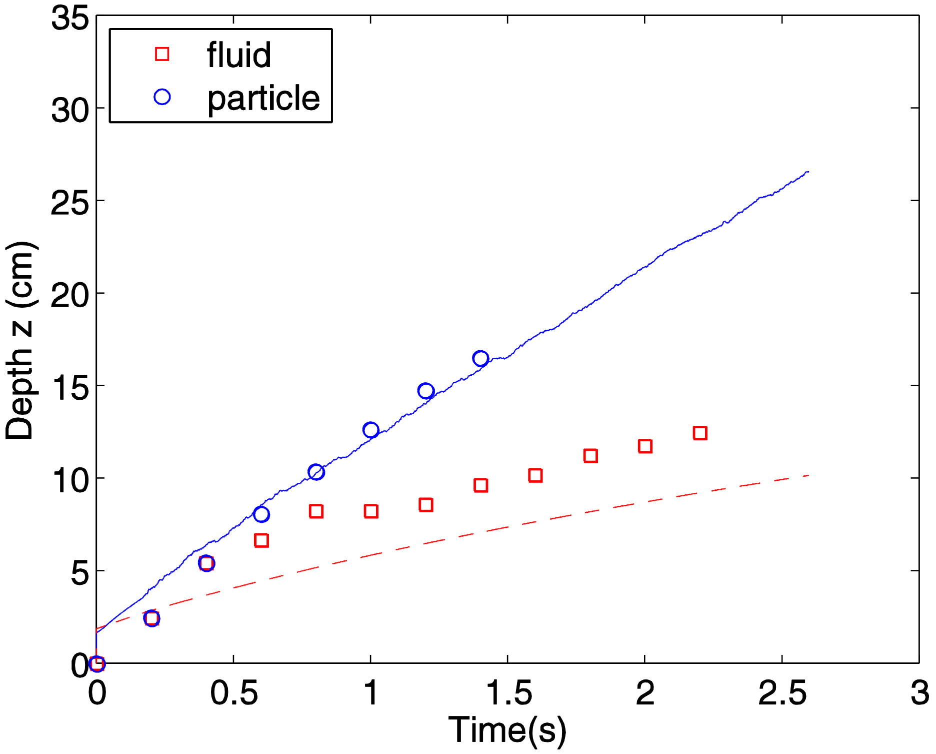
□ fluid
○ particle
Depth z (cm)
0
5
10
15
20
25
30
35
Time(s)
0
0.5
1
1.5
2
2.5
3

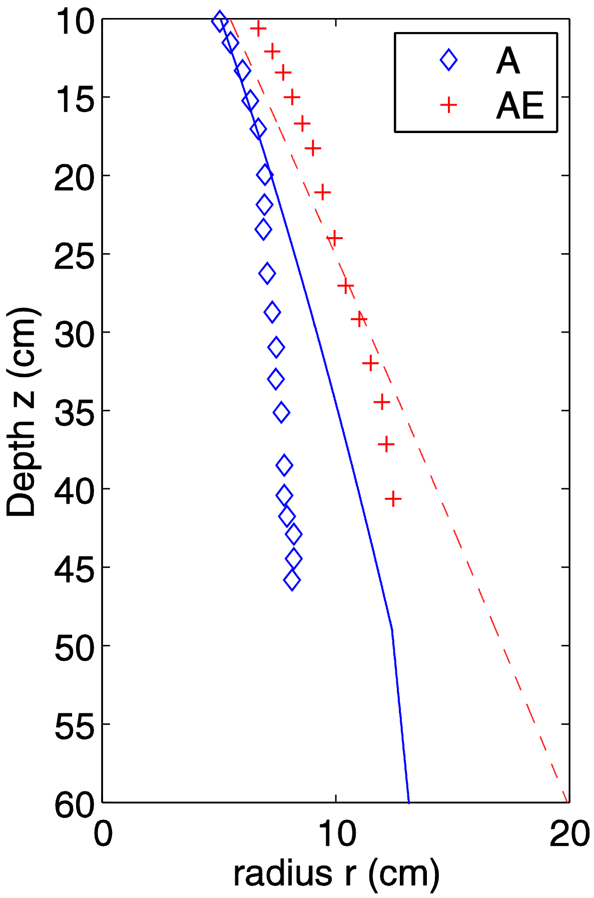

Fig. 1 Trajectory of a layer of particles when an expanding spherical vortex passes through.

Fig. 2 Visualization of the ‘ambient parcel’ (blue symbols) and the entrained ‘thermal parcel’ (red symbols) at t = 6.0s. Initial buoyancy B_o = 0.0414 kg m/s^2. α = 0.25. Actual computations carried out in three-dimensional domain

Fig. 3 Volume of thermal predicted by an integral model (line) and an expanding spherical vortex (symbols). Initial buoyancy B_o = 0.0177 kg m/s^2

Fig. 4 A dense particle cloud in stagnant ambient fluid

Fig. 5 Experimental setup of this study

Fig. 6 Observation in the experimental run with size D: (*a*) t = 0.8s; (*b*) t = 3.3s; (*c*) t = 13.3s; (*d*) t = 26.6s

Fig. 7 Variation of the cloud growth rate with cloud number

Fig. 8 Comparison of model predictions and observation of the shape and size of a particle cloud in an experiment run (size B).(*a*) Model predictions; (*b*) Observation. Time t from left to right: t=1.3 s;t=3.3 s; t=6.6 s; t=13.3 s.

Fig.9 Comparison of model predicted and observed (a) circularity (b) aspect ratio of a sediment cloud along z.

Fig.10 Variation of particle cloud position, size, and shape in 10 runs (size B, t= 3.3 s)

Fig.11 Variation of (*a*) particle cloud front;(*b*) entrained fluid front with time. Line: predictions, symbols: observation (average of five runs). Error bar indicates data range.

Fig.12 Transient variation of the half-width of (*a*) particle cloud; (*b*)entrained fluid. Line: predictions, symbols: observation (average of five runs). Error bar indicates data range.

Fig.13 Comparison of predicted (solid line) and observed (Rahimipour and Wilkinson 1992) characteristics of a particle cloud in the thermal phase. (a) Descend velocity; (b) Growth rate

Fig.14 Comparison of predicted (solid line) and observed (Buhler and

Papantoniou 1991,1999,2001) characteristics of a particle cloud in

the

dispersive phase. (a) Cloud width; (b) Cloud descend velocity

Fig.15 Comparison of predicted (solid line: solid phase; dashed line: fluid phase) and observed cloud descent with time (Luketina and Wilkinson 1998)

Fig.16 Comparison of predicted (solid line: solid phase; dashed line: fluid phase) and observed cloud descent with time (Deguen et al. 2011)

Fig.17 The particle size effect on sediment cloud spreading predicted by the model and its comparison with observation (data from Gensheimer et al. 2012). Mass of release: 40.0 g. Solid line: prediction for size A; dashed line: prediction for size AE (d = 0.120 mm).

Type	Median d (mm) (range)	ρ_s (g/cm^3)	l_{at} (cm)	l_{ts} (cm)
A	0.725 (0.600 - 0.850)	2.5	1.44	4.0
B	0.513 (0.425 - 0.600)	2.5	1.44	5.9
D	0.256 (0.212 - 0.300)	2.5	1.44	14.4

Table 1 Properties of particles used in this study